

1 **The SWI/SNF PBAF complex facilitates REST**
2 **occupancy at repressive chromatin**

3

4 Elena Grossi^{1,2,3,6*}, Christie B. Nguyen^{1,2,3,4,6}, Saul Carcamo^{3,5}, Shannon Moran^{1,2,3}, Valentina
5 Kirigin Callaú^{1,2,3}, Dan Filipescu^{1,2,3}, Dan Hasson^{1,2,3,4,5}, Emily Bernstein^{1,2,3,4*}

6

7 ¹Department of Oncological Sciences, ²Department of Dermatology, ³Tisch Cancer Institute,
8 ⁴Graduate School of Biomedical Sciences, ⁵Bioinformatics for Next Generation Sequencing
9 (BiNGS) Shared Resource Facility, Icahn School of Medicine at Mount Sinai, New York, NY, USA

10

11 ⁶Equal contribution

12 *Co-corresponding authors

13

14 Correspondence should be addressed to emily.bernstein@mssm.edu ; elena.grossi@mssm.edu

15

16

17 **Summary**

18 Multimeric SWI/SNF chromatin remodelers assemble into discrete conformations with unique
19 complex functionalities difficult to dissect. Distinct cancers harbor mutations in specific subunits,
20 altering the chromatin landscape, such as the PBAF-specific component ARID2 in melanoma.
21 Here, we performed comprehensive epigenomic profiling of SWI/SNF complexes and their
22 associated chromatin states in melanoma and melanocytes and uncovered a subset of PBAF-
23 exclusive regions that coexist with PRC2 and repressive chromatin. Time-resolved approaches
24 revealed that PBAF regions are generally less sensitive to ATPase-mediated remodeling than
25 BAF sites. Moreover, PBAF/PRC2-bound loci are enriched for REST, a transcription factor that
26 represses neuronal genes. In turn, absence of ARID2 and consequent PBAF complex disruption
27 hinders the ability of REST to bind and inactivate its targets, leading to upregulation of synaptic
28 transcripts. Remarkably, this gene signature is conserved in melanoma patients with ARID2
29 mutations. In sum, we demonstrate a unique role for PBAF in generating accessibility for a
30 silencing transcription factor at repressed chromatin, with important implications for disease.

31 **Keywords**

32 SWI/SNF, PBAF, ARID2, REST, melanoma

33 Introduction

34 The mammalian SWItch/Sucrose Non-Fermentable (SWI/SNF) complexes are multimeric
35 chromatin remodelers that utilize the energy of ATP hydrolysis to mobilize nucleosomes and
36 provide an accessible chromatin substrate for transcription factors (TFs) and RNA Polymerase II
37 (Pol II) machinery^{1,2}. Recent structural and biochemical studies have unveiled important details
38 regarding SWI/SNF complex composition, as well as how these complexes engage the
39 nucleosome octamer³⁻⁶. Nevertheless, the mechanisms by which chromatin remodelers that lack
40 sequence-specific DNA binding ability recognize specific genomic targets, remains unclear. While
41 *in vitro* studies point towards histone modifications and chromatin states dictating SWI/SNF
42 binding and remodeling activity⁷, recent *in vivo* evidence suggests a more dynamic mechanism,
43 whereby these complexes scan the genome, transiently engaging the nucleosome, and
44 productively remodel chromatin only when interacting with specific TFs^{8,9}. Importantly, various
45 TFs rely on distinct families of chromatin remodeling complexes (e.g. SWI/SNF or ISWI) for proper
46 genomic binding¹⁰, highlighting a co-dependency between these chromatin components.

47 Further complicating the functional dissection of individual SWI/SNF complexes is the modular
48 nature of these macromolecular assemblies, that generally exist in three distinct conformations,
49 known as canonical BAF (cBAF), non-canonical BAF (ncBAF), and Polybromo-associated BAF
50 (PBAF)⁶. These three complex subfamilies are characterized by unique components, as well as
51 several common core subunits including an ATPase module, whose catalytic activity is
52 continuously required to maintain chromatin accessibility, especially at enhancer elements¹¹⁻¹⁴.
53 SWI/SNF remodeling, particularly by cBAF, also mediates the rapid eviction of Polycomb
54 Repressive Complexes (PRC1/2) and in turn, their associated histone marks (H2AK119ub and
55 H3K27me3, respectively), establishing accessible chromatin within minutes of its occupancy^{15,16}.
56 Moreover, different SWI/SNF complexes preferentially bind distinct regulatory regions of the
57 genome, with PBAF mainly enriched at promoters and cBAF primarily occupying enhancers¹⁷.
58 However, the molecular basis governing these preferences remains unclear, as most studies
59 elucidating SWI/SNF mechanisms of action have focused on common SWI/SNF complex
60 subunits (e.g., the enzymatic subunit BRG1/SMARCA4), and are therefore unable to discriminate
61 between distinct complex subfamilies or uncover potential functional differences.

62 Understanding how each SWI/SNF remodeling complex operates is of paramount importance,
63 particularly in the context of human disease. While mutations in SWI/SNF subunits are collectively
64 found in >20% of human cancers, genetic alterations in individual components are enriched in

65 distinct tumors rather than randomly distributed across cancer types, suggesting lineage- and
66 subunit-specific functions¹⁸⁻²⁰. For instance, the PBAF-specific component ARID2 is considered a
67 mutational ‘cancer driver’ in melanoma²¹⁻²⁴, an aggressive skin cancer derived from melanocytes.
68 ARID2 alterations are present in 18% of melanoma samples, according to the Cancer Genome
69 Atlas (TCGA) database²⁵⁻²⁷, and are largely missense or nonsense with very few hot spots,
70 pointing towards a tumor suppressive role. Interestingly, ARID2 mutations have been detected in
71 early melanoma lesions²², yet are also enriched in melanoma metastases^{28,29}, suggesting that
72 this factor might be important at different stages of melanoma onset and progression. Recent
73 evidence from our group showed that ARID2 loss-of-function in melanoma impairs PBAF complex
74 assembly, in line with the structural role of ARID subunits in complex formation⁶. This leads to
75 BAF genomic redistribution, ultimately resulting in activation of transcriptional programs
76 associated with melanoma cell dissemination³⁰. Nevertheless, it remains unclear whether PBAF
77 utilizes unique molecular mechanisms distinct from other SWI/SNF complexes that are essential
78 in specific developmental and/or tumoral contexts.

79 To address this question, we carried out comprehensive epigenomic profiling of the SWI/SNF-
80 associated chromatin landscape in melanoma cells and primary normal human epidermal
81 melanocytes (NHEM). We found that PBAF-enriched regions exhibit lower levels of chromatin
82 accessibility than cBAF and ncBAF sites, and a subset of PBAF occupied regions are
83 unexpectedly enriched for H3K27me3 and the PRC2 complex. By employing a SWI/SNF chemical
84 inhibitor in a time-resolved fashion, we further revealed that PBAF regions are less sensitive to
85 ATPase-dependent remodeling than those of BAF, with different response rates associated with
86 distinct sets of TFs. Among them, we identified the transcriptional repressor REST (RE1 Silencing
87 Transcription Factor) as a PBAF-specific TF enriched at inactive regions, and whose chromatin
88 occupancy is dependent on PBAF. Accordingly, REST target genes are derepressed upon ARID2
89 depletion, as well as in human melanoma tumors bearing ARID2 mutations, unveiling a molecular
90 crosstalk between a chromatin remodeler with modest remodeling activity and a repressive TF at
91 inactive chromatin.

92 **Results**

93 **A subset of PBAF-enriched regions associates with repressed chromatin**

94 We previously demonstrated that in the absence of functional PBAF complexes in melanoma,
95 BAF redistributes genome-wide, ultimately affecting chromatin accessibility and TF binding³⁰. This

96 suggests a delicate balance between SWI/SNF subcomplexes and their associated TFs. To
97 characterize genomic regions uniquely regulated by SWI/SNF complexes, as well as their
98 associated epigenetic landscapes, we performed genomic mapping studies in melanoma cells
99 and NHEM (**Fig. 1A, B**). PBAF-enriched genomic regions were defined as loci bound by the
100 PBAF-exclusive subunit ARID2, but lacking SS18, a SWI/SNF subunit present only in cBAF and
101 ncBAF complexes⁶. Shared regions were characterized by occupancy of both ARID2 and SS18,
102 while cBAF/ncBAF (referred to as BAF) showed exclusive enrichment for SS18 (**Fig. 1A, B; Table**
103 **S1**).

104 By profiling a variety of active and repressive histone modifications in two melanoma cell lines
105 with distinct driver mutations, 113/6-4L (herein referred to as 4L; BRAF^{V600E}) and SKmel147
106 (NRAS^{Q61R}), we confirmed the observation that PBAF is enriched at active promoters (marked by
107 H3K4me3) but less so at functional enhancers (marked by H3K4me1), while BAF primarily binds
108 enhancers, and shared regions encompass both regulatory elements (**Fig. 1A, S1A, B**)³⁰.
109 Interestingly, the PBAF binding profile was somewhat distinct in NHEM, displaying enrichment at
110 both proximal and distal regulatory regions of the genome (**Fig. S1B**). In addition, H3K4me3 levels
111 at PBAF-exclusive regions appeared drastically reduced in NHEM, whereas they remained high
112 at shared sites. While the reduction in H3K4me3 might be associated with the global decrease of
113 this histone modification upon cellular differentiation^{31,32}, the concomitant increased proportion of
114 shared regions in NHEM vs. melanoma might also indicate that in differentiated cells, the PBAF
115 complex relies on the presence of BAF to exert its role at promoters (**Fig. 1B, S1B**). Nonetheless,
116 in both normal and tumor cells, a large fraction of these regulatory elements was marked by
117 H3K27ac, with shared regions (i.e., BAF/PBAF-bound promoters) exhibiting the highest
118 enrichment.

119 Notably, at a subset of PBAF-enriched regions lacking H3K27ac, we unexpectedly identified
120 enrichment of H3K27me3, a mark deposited by PRC2 (**Fig. 1A, B, S1A**). This feature was not
121 exclusive to tumor cells, as we observed even higher H3K27me3 enrichment at PBAF-exclusive
122 regions in NHEM compared to melanoma cells (**Fig. 1B**). This was not the case for H3K9me3, a
123 histone modification associated with constitutive heterochromatin (**Fig. 1A, B, S1A**). Consistently,
124 chromatin state models generated with ChromHMM³³ revealed that ~3% of PBAF peaks in
125 melanoma cells (4L and SKmel147), and 11% in melanocytes, occupy regions exclusively marked
126 by H3K27me3 (**Fig. 1C, S1C, D**). In comparison, only 0.2-0.8% and 1% of BAF sites (in melanoma
127 and melanocytes, respectively) colocalize with this repressive mark. The higher enrichment found
128 in NHEM might reflect the more repressed epigenome of differentiated cells³⁴, in particular at

129 regulatory regions of the genome, as some H3K27me3 was also observed in shared and BAF-
130 enriched regions in NHEM (**Fig. 1B, C**). These results, obtained by H3K27me3 CUT&RUN, were
131 further validated by ChIP-seq using an unrelated H3K27me3 antibody (**Fig. S1E, F**). Taken
132 together, these data suggest that PBAF and PRC2 may co-exist at certain chromatin loci, in
133 contrast with the previously described antagonistic relationship between the BAF and PRC
134 complexes^{15,16}.

135 Next, we aimed to confirm occupancy of the PRC2 complex at these H3K27me3-marked regions.
136 To do so, we mapped the genomic binding of the PRC2 catalytic subunit EZH2 and found it was
137 indeed enriched at PBAF-specific regions in both normal and tumor cells (**Fig. 1D, S1E, G**). As
138 expected, PBAF is associated with far fewer H3K27me3 sites than EZH2, yet a subset of PBAF
139 regions present similar levels of H3K27me3, while BAF and shared regions display greatly
140 reduced levels (**Fig. 1E, S1H**). Lastly, ChIP-seq for the core catalytic SWI/SNF component BRG1
141 and the PBAF-specific subunit PBRM1 confirmed that PBAF-enriched repressed regions are
142 indeed bound by fully assembled PBAF complexes (**Fig. 1D, S1A, E, G**), as PBRM1 is one of the
143 last subunits to be assembled into PBAF and no partially assembled complexes containing
144 PBRM1 have been identified⁶. These data collectively indicate that PBAF can co-localize with
145 PRC2 at a subset of repressed genomic regions devoid of the BAF complex.

146 **PBAF-enriched regions exhibit lower levels of chromatin accessibility than those of BAF**

147 Since PRC eviction from chromatin can be mediated by the ATPase-dependent remodeling
148 activity of the SWI/SNF complex¹⁵, we tested chromatin accessibility levels across the SWI/SNF
149 regions described above in both normal and transformed cells. Interestingly, we found that
150 accessibility at PBAF-enriched chromatin regions is generally lower compared to shared or BAF
151 sites in all melanoma cell lines examined, as well as in NHEM (**Fig. 2A, B, S1A**). We then asked
152 whether occupancy levels of either BAF or PBAF complexes correlated with accessibility status
153 at their respective bound regions. We found that while SS18 binding presents a strong, positive
154 correlation with chromatin accessibility at BAF loci ($R=0.64$), correlation values are much lower
155 for ARID2 binding ($R=0.31$), indicating that PBAF presence alone is not sufficient to efficiently
156 open chromatin (**Fig. 2C**).

157 While low ATAC-seq signal appears to be a common feature of PBAF-enriched regions, only a
158 subset of these sites displays enrichment of EZH2 and H3K27me3, as shown by k-means
159 clustering of PBAF-enriched peaks in melanoma cells and NHEM (**Fig. S2A, B**). To understand
160 the biological relevance of these PBAF-PRC2 regions, we associated such sites (811 peaks in 4L

161 and 2263 in NHEM) with the nearest gene. RNA-seq analysis in normal and tumor cells revealed
162 that these genes display very low expression levels, in line with their associated chromatin state
163 (**Fig. S2C, D**). Moreover, Gene Ontology (GO) analysis identified significant enrichment for terms
164 related to synaptic transmission, ion channel function, and neuron differentiation in both normal
165 and tumor cells (**Fig. 2D** and **Table S2**). Among these PBAF-occupied, ATAC-low, H3K27me3-
166 enriched repressed genes associated with neuronal function is *ACTL6B*, a member of the
167 neuronal BAF (nBAF) complex, a lineage-specific BAF assembly that is necessary for
168 neurogenesis³⁵ (**Fig. 2E**). Interestingly, melanocytes share a common neural crest precursor with
169 neuronal cells and silencing of neuronal-related genes is a critical step in the establishment of the
170 melanocyte lineage, while their deregulation has been associated with increased malignancy³⁶⁻³⁹.
171 Taken together, these results indicate that PBAF binding at its genomic targets, in the absence of
172 BAF co-occupancy, results in a lower level of chromatin remodeling inferred by chromatin
173 accessibility, thus possibly preserving an inactive or poised status of key developmental genes.

174 **SWI/SNF complex subfamilies present distinct remodeling dynamics**

175 To better understand the differences in remodeling activity of distinct SWI/SNF complexes, we
176 utilized a selective BRG1/BRM ATPase inhibitor (BRM014), which has recently allowed the study
177 of SWI/SNF activity at unprecedented resolution^{12-14,40}. We treated 4L melanoma cells with 1 μ M
178 of BRM014 for 10 minutes, 1 hour, or 6 hours, to temporally resolve the remodeling activity of
179 different SWI/SNF complexes in a short timeframe using ATAC-seq as readout. Importantly, this
180 inhibitor does not affect SWI/SNF chromatin occupancy, nor impacts melanoma proliferation at
181 these time points (**Fig. S3A, B**).

182 Unbiased analysis and k-means clustering of altered ATAC peaks revealed that upon ATPase
183 inhibition, chromatin accessibility at distinct genomic regions is affected at different rates (**Fig.**
184 **S3C**). For example, a large fraction of ATAC peaks is immediately affected by inhibitor treatment,
185 quickly reducing accessibility levels within the first 10 minutes (clusters #2, #4); other clusters
186 lose chromatin opening at a slower rate (clusters #3, #5), while a minimal set of regions increases
187 accessibility (cluster #1). Interestingly, these patterns mirror what was reported in murine
188 models¹², suggesting conserved mechanisms in mammals.

189 By integrating altered ATAC-seq peaks across all time points, we observed a large fraction of
190 regions with reduced accessibility (37%), while gained peaks appear to be a minority (0.7%), and
191 the majority represented by constant regions, which may require other chromatin remodeling
192 factors or prolonged inhibition (**Fig. 3A**). However, when we overlaid these regions with

193 SWI/SNF occupancy, we observed that while SS18 and BRG1 are preferentially bound to
194 decreased ATAC peaks, ARID2 is not. In fact, when we assigned ATAC-seq peaks to either BAF,
195 shared, or PBAF regions, we observed that while BAF and shared sites largely overlap with
196 regions that decrease in accessibility (64.5% and 42.3%, respectively), accessibility at PBAF-
197 enriched loci was reduced in only 6.2% of cases (**Fig. 3B**). This suggests that genomic regions
198 exclusively bound by PBAF are less sensitive to ATP-dependent remodeling inhibition.

199 Next, we examined the dynamics of remodeling across the different time points and the rate of
200 accessibility changes for each SWI/SNF complex. At BAF-enriched regions, ATAC-seq signal is
201 dramatically affected after only 10 minutes of BRM014 treatment and continues decreasing over
202 time, likely reflecting the dependency on ATPase-mediated remodeling of enhancer elements
203 (**Fig. 3C**). Shared BAF/PBAF co-occupied regions lose accessibility at early and intermediate time
204 points but then stabilize at longer stages, possibly reflecting compensation mechanisms by other
205 chromatin remodelers (e.g. EP400/TIP60) at promoter regions¹⁴. In contrast, PBAF-only regions
206 present minimal to no reduction in ATAC signal upon BRM014 treatment, and this minor loss of
207 accessibility occurs with a slower kinetics, requiring 1 hour of treatment.

208 We next asked whether co-occupancy of distinct TFs may play a role in response to ATPase
209 inhibition, as they have been associated with specific sensitivities to ATPase-mediated
210 remodeling. For instance, binding of the pluripotency TF OCT4 is rapidly reduced upon SWI/SNF
211 catalytic inhibition in mouse embryonic stem cells (mESC), while CTCF is unaffected¹². We
212 therefore clustered SWI/SNF-associated ATAC peaks (both constant and affected regions)
213 according to their respective complex and the rate of accessibility change at different time points
214 and performed TF motif enrichment analysis, identifying differences within and between different
215 complexes (**Fig. 3D, E** and **Table S3**). For example, SOX10 is exclusively found at ATPase-
216 dependent, BAF-specific regions, while the MITF and FOSL2 (AP1) motifs are present at both
217 shared and BAF regions but mostly enriched at loci unaffected or mildly altered upon BRM014
218 treatment. Intriguingly, PBAF regions displayed a strikingly different set of enriched TF motifs,
219 including the insulator protein CTCF, characterizing the regions that gain accessibility upon
220 BRM014 treatment, and the transcriptional repressor REST, which demarcates the small portion
221 of ATPase-dependent PBAF regions (**Fig. 3D, E**).

222 To understand whether distinct TFs can affect the remodeling activity of different SWI/SNF
223 complexes, we analyzed data from a recently published study performed in murine mammary
224 epithelial cells¹³, in which PBAF-associated elements were found to be even less sensitive to
225 BRM014 treatment compared to our study (0.1% after a 6-hour treatment). Motif enrichment

226 analysis revealed that BAF-bound sites were associated with the AP1 family of TFs, in line with
227 the role of this TF at enhancers and consistent with our previous results in melanoma cells³⁰ (**Fig.**
228 **S3D-E**). In contrast, PBAF-specific regions were enriched for the TF RONIN/GFY, while no REST
229 motif was found at these sites, possibly explaining the lack of BRM014-sensitive PBAF regions in
230 this cell system. Together, these results suggest that TF composition might influence the
231 remodeling susceptibility of different genomic regions and constitute a discriminating feature to
232 predict how chromatin sites respond to SWI/SNF remodeling inhibition.

233 **The transcription factor REST is preferentially associated with the PBAF complex**

234 Our data point towards different remodeling sensitivities linked to distinct sets of TFs. We
235 previously reported PBAF preference for the REST motif³⁰. To further investigate the association
236 between REST and SWI/SNF complexes, we performed ChIP-seq for this TF in melanoma cells
237 and NHEM and confirmed its enrichment at PBAF-exclusive regions (**Fig. 4A**). Given that REST
238 binds a relatively low number of regions (1556 peaks in melanocytes and 3081 in 4L melanoma
239 cells), the subset of chromatin sites co-occupied by REST and PBAF is small, but it corresponds
240 to the most repressed regions bound by PBAF (**Fig. S4A**). CTCF ChIP-seq in NHEM showed that
241 this TF is localized at another well-defined and non-overlapping subset of PBAF sites, with these
242 two TFs combined covering >25% of PBAF-occupied chromatin regions.

243 Interestingly, REST-bound regions in mESC were previously characterized by their unique
244 response to SWI/SNF chemical inhibition, as they lose accessibility and TF binding at slower rates
245 compared to regions bound by activating TFs¹². We confirmed this slow dynamic in our human
246 cell model (**Fig. S4B**) and linked this distinctive response to the presence of PBAF but no other
247 SWI/SNF complexes (**Fig. 3E**). This connection is more evident when analyzing REST regions;
248 only a limited number of REST peaks are associated with active chromatin marks and the BAF
249 complex, as shown by SS18 binding, in line with its role as transcriptional repressor (**Fig. 4B**,
250 **S4C**). In turn, the majority of REST sites overlap with ARID2 and repressed chromatin marks,
251 such as H3K27me3 and EZH2, indicating that the PBAF complex and REST are functionally
252 connected at inactive regions.

253 Next, we performed reciprocal co-immunoprecipitation (co-IP) using chromatin extracts to
254 evaluate the physical association between PBAF and REST and confirmed that REST pull down
255 enriches for ARID2 and *vice versa* (**Fig. 4C**). This interaction appears to be specific, as SOX10 is
256 not enriched (**Fig. 4C**). Notably, by glycerol gradient sedimentation we observed that REST was
257 enriched at both lighter and heavier fractions, whereas other TFs (such as SOX10 and FOSL2)

258 occupy only the lighter fractions, suggesting that REST can form multiple stable macromolecular
259 complexes (**Fig. 4D**). In line with our co-IP results, REST and ARID2 co-migrated to the heaviest
260 fractions of the gradient, indicating that PBAF might stably interact with this repressive TF (**Fig.**
261 **4D**).

262 Taken together, these data point towards an association between the PBAF complex and REST
263 at repressed PRC2-marked chromatin regions. REST targets related to synaptic function, such
264 as *BSN* and *CHRNA2*, clearly exemplify these regions, presenting binding for PBAF but not BAF
265 subunits, low enrichment of active marks and reduced accessibility, as well as PRC2 occupancy
266 (**Fig. 4E, S4D**).

267 **PBAF loss impairs REST binding at repressed regions**

268 Given the above findings, we sought to investigate whether REST function is affected by loss of
269 the PBAF complex. We therefore deleted ARID2 via CRISPR-Cas9 in melanoma cells and NHEK,
270 as we and others showed that loss of ARID2 disrupts PBAF assembly^{6,30}. Western blot analysis
271 of chromatin extracts revealed that ARID2 knockout (KO) and the consequent PBAF complex
272 disruption (demonstrated by loss of the PBAF-specific component PBRM1), reduced REST levels
273 in chromatin without affecting other SWI/SNF subunits, such as SNF5/SMARCB1 (**Fig. 5A, B,**
274 **S5A**). Interestingly, CTCF levels were not significantly affected in ARID2 KO cells (**Fig. 5A, B**).
275 We therefore speculated that the weak remodeling activity of PBAF is in fact required to enable
276 the binding of REST, but not CTCF, to its target chromatin sites.

277 To test this hypothesis, we performed ChIP-seq for these TFs in melanoma cells and melanocytes
278 depleted of ARID2 and observed a widespread decrease in REST occupancy, while CTCF
279 genomic binding remained unaltered (**Fig. 5C, D, S5B**). Statistical analysis revealed that
280 reduction of REST occupancy affects a large fraction of its binding sites (47%; FDR>0.05;
281 $|\log_2FC|>0.5$) but appears particularly relevant at peaks with high REST binding (**Fig. 5E, F**) as
282 well as peaks localized at repressed regions, which also correspond to the fraction that exhibits
283 the highest ARID2 enrichment (**Fig. 5F**). Constant ($|\log_2FC|<0.5$) and upregulated regions, the
284 latter of which represent a minor fraction of total sites (0.05%), are generally associated with
285 weaker REST binding and are instead enriched in more active chromatin marked by H3K27ac
286 and SS18. Together, these data demonstrate that REST characterizes a specific set of repressed,
287 ATP-dependent PBAF regions, potentially influencing their sensitivity to PBAF remodeling. In turn,
288 PBAF is required to favor REST access to its target sites, pointing towards a dynamic control
289 mechanism of these repressed regions.

290 **PBAF loss triggers derepression of REST targets**

291 Despite the unique functional connection between REST and the PBAF complex, this chromatin
292 remodeler is bound to a much larger set of targets than the transcriptional repressor (**Fig. S4A,**
293 **C**). We therefore sought to investigate whether PBAF-mediated regulation of REST activity
294 impacts gene expression. RNA-seq in WT and ARID2 KO NHEM and melanoma cells revealed
295 different gene expression profiles associated with these distinct cell models (**Fig. 6A, B; Table**
296 **S4**). While melanoma cells up- and downregulated a similar number of genes upon ARID2 loss
297 (459 and 480, respectively), in NHEM, most of the differentially expressed genes (DEGs) were
298 downregulated (370) and only a handful increased their expression (70). Pathway analysis of
299 these datasets revealed little commonality among decreased genes (**Fig. S6A, B; Table S2**),
300 indicating that some genes controlled by PBAF are context dependent. However, among the
301 upregulated genes, we found that both normal and cancer cells increased the expression of REST
302 targets, as shown by TF enrichment analysis (**Fig. 6C, D; Table S2**). These genes belonged to
303 pathways associated to synapse organization and activity, as well as ion channels, in line with the
304 role of REST as repressor of neuronal genes in non-neuronal cells⁴¹⁻⁴⁴. Importantly, we found
305 these pathways enriched in both NHEM and 4L melanoma cells, and similar terms were found in
306 highly invasive SKmel147 melanoma cells depleted of ARID2 in our previous study³⁰.

307 To further understand the transcriptional program co-regulated by PBAF and REST, we performed
308 RNA-seq in REST knockdown (KD) melanoma cells and compared it with ARID2 KO in the same
309 cell line (**Fig. S6C-D; Table S4**). When we directly compared transcripts upregulated upon ARID2
310 or REST depletion, we found that the significant overlapping group included neuronal and
311 synaptic genes (**Fig. 6E, S6E**), indicating that PBAF regulation is critical for this specific set of
312 REST targets.

313 Finally, we sought to extend our analysis to human melanoma patients, given the high rate of
314 ARID2 mutations in this cancer type. We therefore examined public data from the Skin Cutaneous
315 Melanoma (SKCM) TCGA cohort (n=363) and focused on patient samples bearing mutations in
316 SWI/SNF-encoding genes (**Fig. S6F**). We selected the six most highly mutated SWI/SNF
317 components in this cancer type (PBAF-specific ARID2 and PBRM1; BAF-specific ARID1A and
318 ARID1B; core components SMARCA4 and SMARCA2) and compared their gene expression
319 profiles vs. their respective WT samples (**Fig. 6F**). Differential expression analysis revealed that
320 downregulated genes in mutant SWI/SNF samples are often enriched in PRC2 targets,
321 suggesting that genetic alterations in SWI/SNF genes lead to PRC2 overactivation, including in
322 ARID2-mutant samples, and in line with the ARID2 KO transcriptome (**Fig. S6A, B**). However,

323 when we focused on upregulated genes, we found that only samples bearing mutations in ARID2
324 were enriched for REST targets, confirming that even in patients, specific loss of ARID2 function
325 and consequent PBAF impairment reduces the ability of REST to repress its target genes. In
326 conclusion, our data reveals a unique role for PBAF at repressed regions where it facilitates REST
327 binding and silencing activity, a mechanism that is disrupted by ARID2 mutations in melanoma
328 patients.

329 Discussion

330 In recent years, an increasing number of studies have been devoted to identifying and
331 characterizing the biochemical composition, hierarchical assembly, and preference in genomic
332 binding of the SWI/SNF complex subfamilies, yet it remains unclear how the molecular function
333 of these distinct protein assemblies differs. In this study, we elucidated an unappreciated role for
334 the PBAF complex at repressed genomic sites, where its ATPase activity is insufficient to establish
335 active chromatin, but rather is required to facilitate DNA access to the repressive TF REST.

336 Much of our understanding of the SWI/SNF mechanism of action is based on studies that analyze
337 common and/or catalytic complex subunits, such as the ATPase BRG1. This holds true for the
338 concept that SWI/SNF actively evicts Polycomb complexes^{9,15}. To tease apart the specific
339 functions of the PBAF complex, we profiled the epigenomic landscape specifically associated with
340 PBAF regions in melanocytes and melanoma cell models, where this remodeler exerts an
341 important role³⁰. Notably, we found that a subset of PBAF sites was enriched for PRC2 and the
342 H3K27me3 mark that it deposits, challenging the notion that all SWI/SNF subcomplexes are
343 capable of opposing PRC1/2 and restoring active chromatin with the same efficiency. Interestingly,
344 melanocytes demonstrated a higher enrichment for these heterochromatic marks than melanoma
345 cells, possibly reflecting the more condensed chromatin structure characteristic of differentiated
346 cells compared to plastic cancer cells^{34,45}. Consistent with our findings, it was recently reported
347 that cBAF, but not PBAF, could remove Polycomb-associated marks when recruited to the bivalent
348 *Nkx2.9* locus in mESCs⁴⁶, a finding consistent with a lack of PBAF-PRC2 opposition. Moreover,
349 it suggests that our findings are not restricted to the melanocytic lineage.

350 PBAF-specific regions displayed lower chromatin accessibility compared to cBAF/ncBAF-specific
351 or shared sites, suggesting that PBAF remodeling activity is insufficient to properly open its target
352 regions in the absence of other SWI/SNF complexes. Using BRM014 to block SWI/SNF ATPase
353 activity, we found that only a small fraction of PBAF sites responded with reduction in accessibility;
354 conversely, cBAF/ncBAF regions were largely sensitive to BRM014, quickly losing accessible

355 chromatin. Therefore, PBAF displays distinct remodeling dynamics compared to other SWI/SNF
356 subcomplexes. One possibility for this difference in complex behavior is that PBAF's intrinsic
357 structural features limit its ability to efficiently open chromatin in absence of other remodelers *in*
358 *vivo*. Recent cryoEM studies that solved BAF and PBAF structures have revealed that these two
359 complexes adopt different conformations to engage the nucleosome^{3,5,47}; yet further studies are
360 needed to understand how these distinct characteristics affect remodeling *in vivo*. Another
361 possibility is that the chromatin features of PBAF-bound sites dictate their poor susceptibility to
362 ATPase-mediated remodeling, as suggested to explain different sensitivities to SWI/SNF
363 chemical inhibition^{13,14}.

364 We speculate that the presence of complex-specific TFs could also contribute to influence
365 remodeling sensitivity at their target regions. In fact, recent evidence indicates that the SWI/SNF
366 complex probes the genome, transiently colocalizing with both active and repressive chromatin
367 marks, and it productively engages and mobilizes nucleosomes only in association with specific
368 TFs^{8,9}. Therefore, we inquired whether different TFs were linked to distinct responses to SWI/SNF
369 inhibition. We found that BAF- and PBAF-unique regions are enriched in different sets of TFs.
370 While BAF sites are enriched in neural crest-specific activating TFs found at promoters and
371 enhancers, such as MTF and SOX10^{48,49}, PBAF regions present unique binding for the insulator
372 protein CTCF and the repressive TF REST. Interestingly, both TFs recognize a large binding
373 motifs of >17 base pairs with high specificity and mediate DNA demethylation^{10,50}; yet they
374 respond differently to remodeling activity. CTCF and REST have been shown to characterize
375 distinctive clusters of genomic regions that respectively increase or slowly decrease chromatin
376 accessibility levels in response to SWI/SNF inhibitors in mESCs¹². We now demonstrate that both
377 CTCF- and REST-enriched clusters are exclusively associated with PBAF regions with unique
378 responses to SWI/SNF inhibition. Importantly, our data suggest caution when using these TFs to
379 generally inform on SWI/SNF function, as they prevalently associate with PBAF, at least in the
380 melanocytic lineage. Moreover, it has been shown that the Imitation Switch (ISWI) family of
381 remodelers is primarily responsible for CTCF binding and establishment of local accessibility^{10,51}.
382 Further studies are therefore needed to clarify whether multiple chromatin remodelers work
383 together at CTCF sites. In addition, we expect different TF-remodeler associations to be found in
384 distinct tissues and/or organisms. By analyzing ChIP-seq data profiling SWI/SNF complexes in
385 mouse mammary epithelial cells¹³, we found the PBAF complex associated with the TF
386 Ronin/GFY, which is also characterized by a large binding motif, suggesting that a unique binding
387 'grammar' might be linked to PBAF occupancy.

388 REST is a silencing TF that we previously linked to PBAF-enriched regions in melanoma cells³⁰.
389 Here we found that this transcriptional repressor characterizes ATPase-sensitive PBAF-specific
390 sites that are enriched in repressive marks. Notably, while CTCF chromatin binding is not affected
391 by ARID2 depletion and consequent PBAF disassembly, REST occupancy is reduced in absence
392 of PBAF, in particular at repressed regions where it colocalizes with this remodeler. REST is a
393 lineage-specific TF that recruits histone deacetylases and methyltransferases to repress neuron-
394 specific genes involved in synaptogenesis, axon guidance and synaptic structure in all non-
395 neuronal cells^{42,52}, but its function is particularly relevant in neural crest cells (NCCs), as they
396 differentiate into many cell types, including neurons and melanocytes^{53,54}. We propose that
397 PBAF's ability to establish limited levels of accessibility at relevant developmental genes is
398 required to enable the binding of silencing factors, such as REST, that in turn ensure a repressive
399 state by recruiting their associated corepressors. In fact, RNA-seq of ARID2 KO melanoma cells
400 and melanocytes revealed the upregulation of a common REST gene expression signature. This
401 demonstrates that PBAF deficiency prevents REST function at its target genes, which in turn
402 results in derepression of neuronal genes. Given the importance of these genes in defining
403 neuronal functions and the observed pigmentation defects in NCC-specific *Rest* conditional KO
404 (cKO) models⁵⁴, we speculate that impairment of PBAF-mediated regulation of REST targets
405 might interfere with proper NCC development and be linked to neurocristopathies. Consistently,
406 PBAF is known to control NCC formation along with CDH7, whose dysfunction causes CHARGE
407 syndrome^{55,56}. However, PBAF function could also be relevant in cancer, as it has been shown
408 that melanoma tumors can form synaptic-like connections with surrounding cells, such as
409 keratinocytes and nerves, to promote tumor growth, angiogenesis and dissemination^{57,58}. In
410 keeping with this idea, melanoma patient samples bearing ARID2 mutations upregulate REST
411 target genes, indicating that ARID2 alterations may predict for this synaptic signature. Future
412 studies will be aimed at determining the functional consequences of this conserved signature and
413 whether it plays a role in promoting melanoma progression and/or allowing adaptation to certain
414 host microenvironments.

415 In conclusion, our study provides insight into the relationship between distinct SWI/SNF
416 remodelers and TFs, whose tissue-specific function might help to explain why genetic alterations
417 in individual SWI/SNF components are enriched in particular tumor types.

418

419

420 **Acknowledgments**

421 The authors thank the laboratory of Roland Friedel for expertise and advice; Ana Hahn and Kevin
422 Mohammed for NGS support; Austin Meadows and Nivetha Aravind for technical support; Ivan
423 Raimondi for advice; the Bernstein lab for discussions and feedback; the Bioinformatics for Next
424 Generation Sequencing (BiNGS) core at the Icahn School of Medicine at Mount Sinai (ISMMS)
425 for bioinformatic support, and the Flow Cytometry core at ISMMS for support with cell sorting.
426 This study was supported by American-Italian Cancer Foundation and National Cancer Center
427 and SBDRRC Transition to Independence Minigrant (funded through NIAMS/NIH SBDRRC P30
428 AR079200-02) to E.G., NIH/NCI F30 CA253988-02 to C.B.N.; American Skin Association to D.F.;
429 and NIH/NCI R01CA154683, MRA Pilot Award for Women in Melanoma Research, and MRF
430 Established Investigator Award to E.B. This work was supported in part by Tisch Cancer Institute
431 of the ISMMS Cancer Center, support grant P30CA196521; Scientific Computing supported by
432 the Office of Research Infrastructure of the NIH under award no. S10OD026880 to ISMMS; and
433 the ISMMS Genomics Technology Facility.

434 **Author contributions**

435 Conceptualization, E.G. and E.B.; investigation, E.G., C.B.N., S.M., V.K.C.; formal analysis, E.G.,
436 C.B.N., S.C., D.H.; writing – original draft, E.G. and E.B.; writing – review & editing, E.G., C.B.N.,
437 S.C., S.M., V.K.C., D.F., D.H. and E.B.; visualization, E.G.; expertise and methods, D.F.; data
438 curation, E.G.; supervision, D.H. and E.B.; funding acquisition, E.G., C.B.N., and E.B.

439 **Declaration of interests**

440 The authors declare no competing interests.

441 **Supplemental information**

442 Document S1. Figures S1–S6

443 Table S1. PBAF-, shared and BAF-enriched regions, related to Fig. 1

444 Table S2. Complete GO analysis, related to Fig. 2 (tab 1), 6 (tab 2, 3) and S6 (tab 4)

445 Table S3. Motif analysis, related to Fig. 2 (tab 1) and S3 (tab 2)

446 Table S4. DEGs in RNA-seq analysis, related to Fig. 6 (tab 1, 2, 4) and S6 (tab 3)

447

448 **Figure legends**

449 **Figure 1.**

450 **A subset of PBAF-enriched regions associates with repressed chromatin.** (A-B) Heatmaps
451 displaying the genomic distribution of the SWI/SNF components ARID2 and SS18, as well as of
452 multiple histone marks, at PBAF-, Shared- or BAF- (cBAF/ncBAF-) enriched regions sorted by
453 H3K27ac signal in (A) 4L melanoma cells or (B) NHEM (see Methods). Black sidebars highlight
454 H3K27me3-rich PBAF regions. (C) Distribution of chromatin states associated with different
455 SWI/SNF subcomplexes and compared to their distribution in the genome of 4L melanoma cells
456 and NHEMs. (D) Metagene profiles of EZH2 and PBRM1 in 4L melanoma cells and EZH2 in
457 NHEM at PBAF-, Shared, or BAF-enriched regions as defined in (A). (E) Violin plot showing the
458 distribution of H3K27me3 signal in 4L melanoma cells at EZH2- (n=37168), PBAF- (n=1241),
459 BAF- (n=1707) enriched or shared (n=58) regions. Only regions overlapping H3K27me3 peaks
460 were selected (see Fig. S1F for unedited data). A pseudocount was added for logarithmic scale
461 visualization. Mean signal for each group was used to calculate fold change (FC) values.
462 Significance was calculated by Mann-Whitney U test.

463 **Figure 2.**

464 **PBAF-enriched regions present a lower level of remodeling activity.** (A) Metagene plots
465 displaying ATAC-seq levels at PBAF-, Shared, or BAF-enriched regions in 4L melanoma cells and
466 NHEM (B) Box plot representing chromatin accessibility levels in 4L melanoma cells (left panel)
467 or NHEMs (right panel) at PBAF-, Shared or BAF-enriched regions. Control (CTRL) sites include
468 ATAC peaks not overlapping with any SWI/SNF region. Significance was calculated by Mann-
469 Whitney U test. (C) Scatter plot showing correlation levels between SS18 or ARID2 levels and
470 ATAC signal at their respective regions. To ensure that only fully assembled SWI/SNF complexes
471 were represented in this analysis, only SS18 and BRG1 or ARID2, PBRM1 and BRG1 overlapping
472 peaks were included as BAF and PBAF regions, respectively. (D) Biological Processes GO
473 analysis of genes localized at repressed PBAF chromatin regions (cluster #1 of Fig. S2A, B) in
474 melanoma cells or NHEMs. (E) Genome browser snapshot showing occupancy of SWI/SNF and
475 PRC2 components, as well as histone marks at *ACTL6B* genomic locus in 4L melanoma cells.

476 **Figure 3.**

477 **Different SWI/SNF subcomplexes display distinct remodeling dynamics.** (A) Heatmap
478 representing accessibility signal in 4L melanoma cells at differentially occupied ATAC regions

479 upon BRM014 treatment, as determined by DiffBind analysis (see Methods). ChIP-seq signal for
480 ARID2, SS18 and BRG1 components is also shown. (B) Pie chart illustrating the percentage of
481 BAF, shared or PBAF regions associated to constant, reduced or gained ATAC peaks, as defined
482 in (A). (C) Metagene profiles showing accessibility changes in 4L melanoma cells at BAF, shared
483 or PBAF regions at different time points of BRM014 treatment. (D) Heatmap illustrating changes
484 in accessibility signal in 4L melanoma cells at BAF, shared or PBAF regions during BRM014
485 treatment. K-means clustering was used to unbiasedly group regions in four clusters. Note that
486 all ATAC regions were included in this analysis, regardless of the significance of the change (E)
487 Heatmap displaying enrichment of selected TF binding motifs from publicly available datasets at
488 different clusters of ATAC regions, as defined in (D). See complete list in Table S3.

489 **Figure 4.**

490 **REST is preferentially associated with the PBAF complex.** (A) Metagene profile of REST
491 ChIP-seq in 4L cells and NHEMs at PBAF-, shared and BAF-enriched regions, as defined in Fig.
492 1A-B. (B) Heatmap displaying REST peaks grouped by k-means clustering, defining active
493 (cluster#1) and inactive (cluster#2) regions in 4L melanoma cells. (C) Western blot analysis of
494 ARID2 or REST immunoprecipitated chromatin extracts in 4L melanoma cells. (D) Immunoblot
495 analysis of glycerol gradient sedimentation from SKmel147 melanoma cells. Different blots
496 performed using the same protein extracts are shown. (E) Genomic browser snapshot illustrating
497 occupancy of SWI/SNF and PRC2 components, histone marks and REST at *BSN* neuronal genes
498 in 4L melanoma cells.

499 **Figure 5.**

500 **PBAF loss impairs REST binding at repressed chromatin regions.** (A-B) Western blot
501 analysis of ARID2 WT and KO chromatin extracts in (A) NHEM and (B) 4L melanoma cells. NTC,
502 non-targeting control sgRNA. LAMIN A/C was used as loading control. (C) Metagene profile of
503 REST and CTCF ChIP-seq in ARID2 WT and KO SKmel147 melanoma cells. (D) Metagene profile
504 of REST ChIP-seq in ARID2 WT and KO NHEMs. (E) MA plot displaying differentially bound REST
505 peaks upon ARID2 KO, as determined by DiffBind analysis. Peaks are plotted according to the
506 extent of the change (fold change KO-WT) and their normalized read density. (F) Heatmap
507 showing REST occupancy in NHEM at differentially bound (Up or Down peaks) or constant REST
508 regions upon ARID2 KO. ChIP-seq signal for ARID2, SS18 and the histone marks H3K27ac and
509 H3K27me3 is also shown at the same regions.

510 **Figure 6.**

511 **PBAF loss triggers derepression of REST target genes.** (A-B) Volcano plots depicting RNA-
512 seq data in ARID2 KO vs. WT (A) 4L melanoma cells and (B) NHEM. (C-D) TF enrichment and
513 Biological Processes GO analyses of genes upregulated (Adj. pvalue <0.05; FC>0.75) upon
514 ARID2 KO in (C) 4L melanoma cells and (D) NHEM. (E) Venn diagram displaying the intersection
515 between upregulated genes in REST KD and ARID2 KO 4L melanoma cells. Overlap significance
516 was calculated by Fisher's exact test. (F) Heatmap showing TF enrichment GO analysis of genes
517 up or downregulated, as determined by differential expression analysis comparing TCGA SKCM
518 samples mutated for one of the listed SWI/SNF component vs. WT samples. *, pvalue<0.05; **,
519 pvalue<0.01; ***, pvalue<0.001; ****, pvalue< 0.0001.

520

521 STAR Methods

REAGENT or RESOURCE	SOURCE	IDENTIFIER
Antibodies		
ARID2	Santa Cruz	sc-166117
ARID2	Cell Signaling	82342 D8D8U
PBRM1	In house	N/A
PBRM1	Bethyl	A700-019
BRD7	Santa Cruz	sc-376180
SS18	Cell Signaling	21792 D6I4Z
SNF5	Santa Cruz	sc-166165
BRG1	Abcam	ab110641
BRG1	Santa Cruz	sc-17796
H3K4me3	Abcam	ab8580
H3K4me1	Epcypher	13-0057
H3K27ac	Abcam	ab177178
H3K27me3	Epcypher	13-0055
H3K9me3	Abcam	ab176916
EZH2	Cell Signaling	3147
CTCF	Millipore	07-729
REST	Millipore	07-579
REST	Santa Cruz	sc-374611
SOX10	Proteintech	66786-1-Ig
RCOR1	Millipore	07-455
LAMIN A/C	Sigma	SAB4200236
GAPDH	Santa Cruz	sc-32233
Bacterial and virus strains		
One Shot™ Stbl3™ Chemically Competent E. coli	Invitrogen	C737303
Chemicals, peptides, and recombinant proteins		
BRM/BRG1 ATP Inhibitor-1 (BRM014)	MedChemExpress	HY-119374
DSG	Pierce (ThermoFisher)	20593
Protein A+G magnetic beads	Millipore	LSKMAGAG10
KAPA HiFi DNA Polymerase	Roche	07958838001
Digitonin	Promega	G9441
Illumina Tagment DNA TDE1 Enzyme and Buffer Kit	Illumina	20034197
T4 PNK	NEB	#M0201S
5U/uL Klenow Fragment (3'-5' exo-)	NEB	#M0212S
Quick T4 DNA ligase	NEB	#M2200S
T4 DNA Polymerase	NEB	#M0203S
DNA Polymerase Klenow Fragments	NEB	#M0210S
dNTPs	Roche	11969064001
dATPs	Roche	11889516103
SPRIselect beads	Beckman Coulter	B23318

Critical commercial assays		
Transit-VirusGEN Transfection Kit	Mirus Bio	MIR6700
NEXTFLEX Poly(A) Enrichment Beads	PerkinElmer	NOVA-512992
NEXTFLEX Rapid Directional RNA-seq Kit 2.0	PerkinElmer	NOVA-5198-01
RNeasy Mini Kit	Qiagen	74104
NEBNext Ultra II DNA Library Prep Kit for Illumina	NEB	E7645S
CUTANA™ ChIC/CUT&RUN Kit v4	EpiCypher	14-1048
Deposited data		
Raw and analyzed RNA-sequencing, ATAC-sequencing, ChIP-sequencing and CUT&RUN data		GSE272705
Experimental models: Cell lines		
SKmel147	Eva Hernando Laboratory (NYU)	RRID:CVCL_3876
113/6-4L	Robert Kerbel Laboratory (Sunnybrook Health Sciences Center)	Cruz-Munoz et al., 2008
NHEM SW5	In-house isolation	N/A
NHEM SW11	In-house isolation	N/A
Oligonucleotides		
Non-targeting sgRNA: CACCGTTCCGCGTTACATAACTTAG	Carcamo et al., Cell Rep 2022	N/A
ARID2 sgRNA#1: CACCGAATGGCAAACCTCGACGGGGA	Carcamo et al., Cell Rep 2022	N/A
ARID2 sgRNA#3: CACCGATGATGATGAGGTACCACC		
ARID2 sgRNA#5: CACCGTTTACTACTTGCTAATGCCG	Carcamo et al., Cell Rep 2022	N/A
SCR shRNA: CCGGTCCTAAGGTTAAGTCGCCCTCGCTCGAGC GAGGGCGACTTAACCTTAGGTTTTTG	This study	N/A
REST shRNA#3: CCGGCGAGTCTACAAGTGATCATTCTCGAGAAT GATACACTTGTAGACTCGTTTT	Sigma-Aldrich	TRCN0000014783
REST shRNA#87: CCGGTCAACGAATCTACCCATATTTCTCGAGAAA TATGGGTAGATTCGTTGATTTTTTG	Sigma-Aldrich	TRCN0000432087
Recombinant DNA		
lentiCRISPR v2	Addgene	52961
psPAX2	Addgene	12260
pMD2.G	Addgene	12259
Software and algorithms		
Gen5 (v.3.12) software	Agilent v.3.12	
Prism	Version 10	https://www.graphpad.com

ImageJ	Version 2.1.0/1.53c	https://imagej.nih.gov/ij/index.html
RStudio	Version 1.1.46	https://rstudio.com
Other		

522

523 RESOURCE AVAILABILITY

524 **Lead contact.** Further information and requests for resources and reagents should be directed
525 to and will be fulfilled by the lead contact, Emily Bernstein (emily.bernstein@mssm.edu).

526 **Materials availability.** Reagents used in this study are publicly available or available from the
527 lead contact upon request.

528 **Data and code availability.** Raw and processed data from RNA-seq, ATAC-seq, and ChIP-seq
529 experiments generated in the current study have been deposited in the Gene Expression
530 Omnibus (GEO) repository under the accession number GSE272705. Published ChIP-seq
531 datasets generated in SKmel147 melanoma cell lines and in non-tumoral murine models are
532 available through the GEO repository (accession numbers GSE172383 and GSE226953,
533 respectively). TCGA melanoma data are publicly available in the NCI Genomic Data Commons
534 (GDC) data portal under project ID TCGA SKCM
535 (<https://portal.gdc.cancer.gov/projects/TCGA-SKCM>). This paper does not report original code.

536 EXPERIMENTAL MODELS

537 **Cell culture.** Melanoma cell lines SKmel147 and 113/6-4L were cultured in DMEM supplemented
538 with 10% FBS (R&D System) and 1X penicillin-streptomycin (Gibco). HEK293T cells were used
539 for virus production and were maintained in DMEM supplemented with 10% FBS and 1X penicillin-
540 streptomycin. Primary normal human epithelial melanocytes or NHEM (batches SW5-SW11) were
541 extracted and cultured as described in⁵⁹. Briefly, neonatal foreskins were collected in PBS
542 supplemented with 1X Antibiotic-Antimycotic (Gibco #15240-062), and stored at 4C for no longer
543 than 48 hr. Skins were then washed once in 70% EtOH and 3x in PBS supplemented with 1X
544 Antibiotic-Antimycotic, cut into 3-4 pieces in HBSS (Gibco #24020-117) and placed in Dispase II
545 solution (Roche #04942078001) at 4C O/N. Epidermis was then separated from the dermis in
546 HBSS, floated in 1 ml of 0.25% trypsin (Gibco #15400-054), and incubated in 37C for 3 min.
547 Detached cells were then collected in 4 mL of DMEM with 10% FBS and spun at 1200 rpm for 5
548 min. The last step was repeated a second time and the two cell pellets were consolidated and
549 resuspended in Melanocyte Growth Media 254 supplemented with Human Melanocyte Growth

550 Supplement (HMGS, Life Technologies #S-016-5) and 0.2 mM CaCl₂, for 3-5 days. Cells were
551 then rinsed in PBS, 1:100 Anti-Anti, and trypsinized in 1 ml 0.05% Trypsin for exactly 3 min to
552 separate melanocytes from fibroblasts and keratinocytes. Cells were then collected into 4 mL of
553 DMEM with 10% FBS, spun at 1200 rpm for 5 min and resuspended and cultured in Melanocyte
554 Growth Media 254 supplemented with HMGS, 0.2 mM CaCl₂, and 10 ng/ml PMA (Sigma
555 #P8139).

556 **METHOD DETAILS**

557 **Plasmid and infections.** For CRISPR-mediated knockout in melanoma cells and primary
558 melanocytes, gRNAs targeting *ARID2* and well as non-targeting control (NTC) gRNAs were
559 cloned into the lentiCRISPRv2 (Addgene #52961). For REST knockdown experiments, shRNAs
560 constructs provided in a pLKO.1 lentiviral backbone were obtained from the RNAi Consortium
561 (TRC, Open Biosystems). Scrambled (SCR) shRNA was used as control. For gRNA and shRNA
562 sequences, see Table S4. To produce lentiviral particles, HEK293T cells were seeded in 10 cm
563 tissue culture dishes and co-transfected with 5 µg of lentiviral expression constructs, 3.75 µg of
564 psPAX2 and 1.25 µg pMD2.G vectors using the TransIT-VirusGen (Mirus Bio) transfection reagent
565 diluted in Opti-MEM medium (Gibco), following manufacturer's recommendations. 48 hours post-
566 transfection, supernatants were collected and passed through a 0.45 µm PVDF filter to remove
567 cells and debris. Upon infection, cells were selected with puromycin (1 µg/ml). For CRISPR-
568 mediated knockout in melanoma cells, limiting dilutions were used to generate colonies from
569 single cells. Individual colonies were isolated and further expanded prior to screening by
570 immunoblot. For primary melanocytes, infected cells were kept as pool, without isolating single
571 clones. KO cell lines are identified by the sgRNA used followed by the clone number, when single
572 clones were isolated (e.g., KO#1.17).

573 **Cell growth assay.** To test cell growth upon BRM014 treatment, 2×10^3 4L melanoma cells were
574 plated into black polystyrene 96-well plates with clear flat bottom (Agilent) in triplicate. BRM014
575 inhibitor was added 24h post plating. Plates were imaged on brightfield every 6h in a 48h time
576 course with a 4X PL FL magnification in a Cytation 7 automated microscope (Agilent). Cell count
577 was performed using the Gen5 (v.3.12) software (Agilent), normalizing each measurement to time
578 0. Growth curves were plotted on GraphPad Prism version 10 (GraphPad Software) using
579 normalized cell counts.

580 **Whole-cell protein extraction and chromatin fractionation.** Chromatin fractionation was
581 performed as described⁶⁰. Briefly, cell pellets were lysed on ice for 8 min in Buffer A (10 mM

582 HEPES pH 7.9, 10 mM KCl, 1.5 mM MgCl₂, 0.34 M Sucrose, 10% glycerol supplemented with
583 1:200 protease inhibitors cocktail and 1 mM DTT) + 0.1% Triton X100. Cell extracts were
584 centrifuged for 5 min at 1850 g and the pellets were washed with 1 ml of Buffer A (supplemented
585 with 1:200 protease inhibitors cocktail and 1 mM DTT). Samples were spun down for 5 min at
586 1850 g and the pellets were resuspended in No Salt Buffer (3 mM EDTA, 0.2 mM EGTA
587 supplemented with 1:200 protease inhibitors cocktail and 1 mM DTT) and incubated on ice for 30
588 min with occasional mixing. Nuclear extracts were centrifuged for 5 min at 1850 g and chromatin
589 pellets were resuspended in 200 μ l Buffer A (supplemented with 1:200 protease inhibitors cocktail
590 and 1:200 Benzonase). Pellets were solubilized for 15 min at 37C shaking and subsequently used
591 for Immunoblot. For whole-cell protein extraction, cells were lysed in RIPA lysis buffer (50mM Tris-
592 HCl pH8, 150mM NaCl, 1% NP-40, 0.5% Sodium deoxycholate, 0.1% SDS supplemented with
593 protease inhibitors cocktail and 1:500 Benzonase) and incubated on ice for 15 minutes with
594 occasional mixing. Lysates were sonicated on high level, 5 cycles 30s ON, 30s OFF and
595 centrifuged at max speed for 10 minutes. Protein concentrations were quantified using
596 Bicinchoninic Acid (BCA) assay (Pierce), according to manufacturer's instructions.

597 **Immunoprecipitation (IP) with chromatin extracts.** Chromatin extracts were prepared as
598 mentioned above using 10-20 \times 10⁶ cells per IP. After BCA quantification, chromatin extracts were
599 diluted in Buffer C (50 mM Tris HCl pH 7.5, 150 mM NaCl, 2mM EDTA, 0.05% NP-40) to equalize
600 protein amounts (e.g. 500 μ g per condition). Diluted extracts were pre-cleared with 20 μ l of Magna
601 ChIP Protein A+G magnetic beads (Millipore) for 1 hours in rotation at 4C and 5% of extract was
602 saved as input. Precleared extracts were then incubated overnight with antibodies (see Table S4),
603 followed by 2 h incubation with 25 μ l of magnetic beads. Beads were subsequently washed once
604 with Buffer G150 (50 mM Tris HCl pH 7.5, 150 mM NaCl, 0.5% NP-40), twice with Buffer G250
605 (50 mM Tris HCl pH 7.5, 250 mM NaCl, 0.5% NP-40) and once with TE buffer and proteins were
606 eluted in 50 μ l of 4X Laemmli loading buffer (Bio-Rad) and boiled 10 minutes at 95C.

607 **Glycerol gradient sedimentation.** Glycerol gradient sedimentation was performed according
608 to⁶¹. 40-50 million melanoma SKmel147 cells were collected, lysed in Nuclear isolation buffer (20
609 mM HEPES pH 7.9, 25 mM KCl, 10% glycerol, 5 mM MgCl₂, 0.05 mM EDTA, 0.1% NP-40, 100
610 nM PMSF, supplemented with protease inhibitors) and washed once with the same buffer without
611 NP-40. The nuclear extracts were then resuspended in Nuclear lysis buffer (10 mM HEPES pH
612 7.6, 3 mM MgCl₂, 100 mM KCl, 0.1 mM EDTA, 10% glycerol). 300 mg/mL of ammonium sulfate
613 powder was added to the mixture and incubated on ice for 20 min. Proteins were pelleted by
614 ultracentrifugation at 150,000 g for 30 minutes and resuspended in 100 mL of HEG1000 buffer

615 (25 mM HEPES pH 7.6, 0.1 mM EDTA, 12.5 mM MgCl₂, 100 mM KCl, supplemented with
616 protease inhibitors). A glycerol gradient (10-30%) was prepared using HEG1000 buffer without
617 glycerol and with 30% glycerol. Next, the protein lysates were layered on top of the 10-30%
618 glycerol gradients (10 mL) and fractionated by centrifugation at 40,000 rpm for 16 h using a
619 SW32Ti rotor (Beckman Coulter). Fractions (20x) of 500 mL were collected sequentially from the
620 top of the gradient, diluted with Laemmli loading buffer and boiled for 10 minutes before being
621 used for immunoblotting.

622 **Immunoblotting.** Protein lysates were mixed with 2X or 4X Laemmli loading buffer supplemented
623 with 2-mercaptoethanol and boiled at 95C for 5 min prior to immunoblotting. Samples were run
624 on a NuPAGE Bis-Tris 4-12% precast gels (Invitrogen) and wet transferred onto a PVDF
625 Immobilon transfer membrane (Millipore) for 1 hour at 30V using Bis-Tris transfer buffer with 20%
626 methanol for high molecular weight targets. Membranes were first incubated with Amido Black to
627 verify uniform loading and incubated with blocking buffer (5% Blotting-grade Blocker (Bio-Rad) in
628 Tris-Buffered Saline, 0.1% Tween (TBS-T)) for 1 hour, followed by overnight incubation with the
629 respective primary antibodies (listed in Table S4). The next day membranes were incubated with
630 the respective secondary antibodies, rinsed with TBS-T, and developed using Clarity Western
631 ECL Substrate (Bio-Rad).

632 **Chromatin Immunoprecipitation (ChIP-seq).** ChIP samples were processed as previously
633 described^{30,59} with modifications. To detect histone modifications, 10-15×10⁶ cells per condition
634 were crosslinked directly on plate with 1% Formaldehyde for 10 minutes at room temperature.
635 For chromatin remodeler subunits and transcription factors, 10-40×10⁶ cells were double cross-
636 linked with 0.25 M disuccinimidyl glutarate (DSG), followed by 1% formaldehyde. Single and
637 double crosslink reactions were quenched with 0.125 M glycine for 5 minutes at room
638 temperature, cells were thoroughly washed with PBS and scraped off the plates in 1 ml ice-cold
639 PBS. Chromatin was then aliquoted and pelleted at up to 1500 g for double crosslinked cells at
640 4C and stored at -80C or used directly for ChIP. Nuclei were isolated by resuspending cell pellets
641 in 10ml of Cell Lysis Buffer (10mM Tris pH 8.0, 10mM NaCl, 0.2% NP-40 supplemented with 1:200
642 protease inhibitors cocktail and 1:2000 DTT) rotating for 10 min at 4C and spun down at 2000g
643 for 10 min at 4C. 15. Nuclear pellets were then resuspended (400µL/10M cells) in Nuclear Lysis
644 Buffer (50mM Tris pH 8.0, 10mM EDTA pH 8.0, 1% SDS supplemented with 1:200 protease
645 inhibitors cocktail and 1:2000 DTT) and incubated on ice with frequent mixing. Cells were
646 sonicated for 20-30 cycles, 30 secs on, 30 secs off, at low (single crosslink) or high (double
647 crosslink) intensity in a Bioruptor sonicator (Diagenode). After sonication, samples were

648 centrifuged at max speed for 10 minutes at 4C, and the supernatant-containing chromatin was
649 diluted 1:4 with IP Dilution buffer (20 mM Tris pH 8, 2 mM EDTA, 150 mM NaCl, 1% Triton-X,
650 0.01% SDS, 100 nM PMSF, supplemented with protease inhibitors). Where indicated, Drosophila
651 spike-in chromatin was added to the diluted chromatin, followed by pre-clearing with Magna ChIP
652 Protein A+G magnetic beads (Millipore) for 2 hours rotating at 4C. 50 μ l of chromatin was saved
653 for input control and chromatin extracts were incubated with the designated antibody O/N in
654 rotation at 4C (ChIP-seq antibodies are listed in Table S4). The following day, 50 μ l of magnetic
655 beads per condition were washed and incubated with the antibody-containing extract for 2 hours
656 rotating at 4C. Beads were then washed once with cold IP Wash I buffer (20 mM Tris pH 8, 2 mM
657 EDTA, 50 mM NaCl, 1% Triton-X, 0.1% SDS, supplemented with protease inhibitors cocktail),
658 twice with cold High Salt buffer (20 mM Tris pH 8, 2 mM EDTA, 500 mM NaCl, 1% Triton-X, 0.01%
659 SDS, supplemented with protease inhibitors cocktail), once with cold IP Wash II buffer (10 mM
660 Tris pH 8, 1 mM EDTA, 0.25 LiCl, 1% NP-40, 1% deoxycholic acid, supplemented with protease
661 inhibitors cocktail) and twice with cold TE buffer (5 mM Tris pH 7.4, 1 mM EDTA). DNA was eluted
662 and reverse crosslinked at 65C with mixing in 50 μ l of Elution Buffer (300mM NaCl, 1% SDS,
663 100mM NaHCO₃) + 2 μ l RNase A for 2 hours, followed by overnight incubation at 65C with 2.5
664 μ l of Proteinase K. DNA was isolated by 2.5X of SPRI beads (Beckman Coulter), following
665 manufacturer's instructions. Library preparation for multiplexes sequencing was carried out
666 according to Illumina's recommendations. 1-8ng of DNA input or ChIP DNA was end-repaired with
667 T4 DNA polymerase (NEB), DNA polymerase I, large (Klenow) fragment (NEB) and T4
668 polynucleotide kinase (NEB) in the presence of deoxyribonucleotide triphosphates (dNTPs)
669 (Roche). Next, dA-tailing was done using Klenow fragment (3'→5' exo-, NEB) with
670 deoxyadenosine triphosphate (dATP) (Roche) in NEB Buffer 2. Barcoded Illumina Truseq
671 adaptors were ligated using Quick Ligase (NEB). Libraries were amplified using KAPA HiFi DNA
672 Polymerase (KAPA Biosystems), with optimal number of cycles determined by qPCR, and size
673 selected using SPRI beads. Resulting libraries were quantified by Qubit (Thermo Fisher) and
674 average DNA fragment size was calculated using an Agilent bioanalyzer or Tape Station system.
675 Libraries were then multiplexed and sequenced on a NextSeq500/550 or NExtSeq2000
676 instrument (Illumina) at 75bp single-end or paired-end reads.

677 **Cleavage Under Targets & Release Using Nuclease (CUT&RUN).** CUT&RUN was performed
678 using CUTANA ChIC/CUT&RUN kit (Epiccypher #14-1048) following manufacturer's protocol.
679 Briefly, 5×10^5 cells were coupled with Concanavalin A beads, permeabilized with 0.01% Digitonin
680 and incubated overnight at 4C with 0.5 μ g target antibody in antibody buffer (antibodies listed in

681 Table S4). The following day, cells were first incubated for 10 minutes with micrococcal nuclease
682 fused to proteins A and G (pAG-MNase), which was then activated by CaCl₂ addition. After 2h
683 incubation at 4C, the reaction was stopped with stop buffer and E. coli DNA was added as spike-
684 in DNA. The DNA was then isolated using SPRI beads and quantified with Qubit. Libraries were
685 prepared using NEBNext Ultra II DNA library kit, following manufacturer's recommendations.
686 Fragment size was detected using a Tape Station system and multiplexed libraries were
687 sequenced on a NExSeq2000 instrument (Illumina) at 50bp paired end reads.

688 **Assay for Transposase-Accessible Chromatin (ATAC-seq).** The Omni-ATAC protocol was
689 used to profile chromatin accessibility⁶² with minor modifications. 5×10⁴ cells were harvested,
690 treated with Digitonin (Promega) and tagmented with 2.5 μl of TDE1 Enzyme (Illumina). The
691 correct number of amplification cycles was determined by qPCR and resulting libraries were
692 isolated and size selected using SPRI beads. Libraries were quantified by Qubit and average DNA
693 fragment size was determined using an Agilent bioanalyzer or Tape Station system. Multiplexed
694 libraries were then sequenced on Illumina NextSeq2000 at 50bp paired-end reads. For ATAC-seq
695 upon ATPase inhibitor treatment, samples were treated with 1 μM of BRM014 compound
696 (MedChemExpress) starting the treatment at different time points, such that all the samples could
697 be collected at the same time.

698 **RNA-seq.** Total RNA was extracted from about 2-4×10⁶ cells using the RNeasy Mini Kit (Qiagen)
699 according to manufacturer's protocol, including DNase digestion. 1-2 μg of total RNA was used
700 to isolate poly-A RNA with NEXTFLEX Poly(A) beads 2.0 (Perkin Elmer), while libraries were
701 prepared using the NEXTFLEX Rapid Directional RNA-seq Kit 2.0 (PerkinElmer). Samples were
702 quantified by Qubit and quality was assessed by Agilent bioanalyzer or Tape Station system.
703 Multiplexed libraries were sequenced on a NextSeq500/550 in a 75bp single-end format.

704 **ChIP-seq and CUT&RUN analysis.** Adapters were trimmed using Trimmomatic (v.0.36)⁶³ or
705 NGmerge (v.0.3)⁶⁴ for single- or paired-end reads, respectively. Reads were aligned to the human
706 reference genome (GRCh38/hg38) using Bowtie2 (v.2.4.1)⁶⁵ with standard parameters, and reads
707 quality was assessed using fastQC. samtools (v.1.9)⁶⁶ was used to generate bam files and filter
708 out low-quality (Phred quality score <30), mitochondrial and duplicated reads. Significant binding
709 peaks were determined using macs2 v2.1.0⁶⁷ for narrow peaks, and SICER 2.0⁶⁸ for broad peaks,
710 with matching input files as control. Cut-off values (q-values) were determined post-hoc, testing
711 several q-values based on signal-to-background ratio and using macs2 --cutoff-analysis parameter
712 for additional guidance. Peaks located in ENCODE blacklisted regions were excluded. Coverage
713 tracks (bigwig files) were generated from filtered bam files using deepTools (v. 3.5.1)⁶⁹

714 bamCoverage with parameters `--normalizeUsingRPGC --binsize 10`. Metagene plots and
715 heatmaps showing signal enrichment over genomic regions were generated by first calculating
716 intensity scores for each genomic site using deepTools `computeMatrix`, and then plotting
717 heatmaps and/or metagene plots with `plotHeatmap`, selecting the center of the peaks as reference
718 point. To remove non-specific signal from accessible chromatin in EZH2 CUT&RUN, ATAC signal
719 was subtracted using deepTools `bigwigCompare` with the following parameters: `--operation ratio -`
720 `--scaleFactors 1:0.01`. To precisely quantify H3K27me3 read intensity at SWI/SNF and EZH2
721 regions, the matrix containing scores per genomic regions calculated with `computeMatrix` was
722 exported and plotted in R studio. Significance was calculated by Mann-Whitney U test using the
723 `wilcox.test` function in R.

724 To identify PBAF-enriched, shared and BAF-enriched regions, ARID2 and SS18 peaks in 4L and
725 SKmel147 melanoma cells and SW11 melanocytes were called using `macs2` and compared using
726 `bedtools (v.2.29.2)`⁷⁰ `intersect`. The regions are listed in Table S1. The `CHIPSeeker 1.34.1`
727 package⁷¹ was used to annotate peaks and to determine their feature distribution. Promoters were
728 defined as $\pm 1\text{Kb}$ from TSS using the annotation package
729 `TxDb.Hsapiens.UCSC.hg38.knownGene`. Chromatin state modeling was performed using the
730 chromatin Hidden Markov Model (`chromHMM`) software as previously described^{33,72}. The overlap
731 between each state and SWI/SNF peaks was calculated using `bedtools intersect`.

732 For differential binding analysis, bam files generated in ARID2 WT and KO samples were
733 analyzed along with matching input files using `DiffBind (v. 3.4.11)`⁷³, following the package
734 documentation

735 (<http://bioconductor.org/packages/release/bioc/vignettes/DiffBind/inst/doc/DiffBind.pdf>). Briefly, a
736 binding matrix was generated with `dba.counts (summits=250)`. Drosophila spike-in data were
737 used for normalization when available, otherwise count normalization was performed using the
738 `DBA_NORM_NATIVE` parameter with `background=T`. `DESeq2` was used to perform differential
739 peak analysis (`FDR<0.05 & |log2FC|>0.5`) and generate MA plots. For visualization purposes, the
740 bam files of WT and KO samples were merged into a master file using `samtools merge`. Significant
741 peaks were called on this merged file using `macs2` with matching input as control and individual
742 coverage tracks were normalized by using `DESeq2` scaling factors. Scaled tracks were then
743 plotted with deepTools `plotHeatmap` to show change in binding at merged peaks.

744 **ATAC-seq analysis.** Adapter trimming, alignment, read filtering and genome coverage
745 calculation were performed as in `ChIP-seq` and `CUT&RUN`. ATAC-seq bam files were merged,
746 and peaks were identified as in¹², by first converting the paired-end bam files to single-end bed

747 format and then running macs2 callpeak function with --shift -100 --extsize 200 parameters. Peaks
748 located in ENCODE blacklisted regions were excluded. For analysis of differentially accessible
749 regions upon BRM014 treatment, two biological replicates for each time point were performed.
750 DiffBind was employed to compare treated samples to the DMSO control sample, as for ChIP-
751 seq data but using the summit=100 parameter to generate the count matrix. ATAC-seq peaks
752 were considered gained or reduced if their accessibility levels were affected at any time point, as
753 calculated by DESeq2 (FDR<0.05 & |log₂FC|>1). Constant and changing ATAC-peaks were
754 associated to SWI/SNF regions (Table S1) using bedtools window (-w 500). Metagene plots
755 showing change in chromatin accessibility at different SWI/SNF regions were generated by using
756 deepStats (v. 0.3.1 - <https://doi.org/10.5281/zenodo.3336593>) dsCompareCurves and bigwig files
757 normalized according to DESeq2 scaling factors. Heatmaps depicting changes in ATAC-seq
758 peaks over time were generated with ggplot2. Regions were grouped by k-means clustering in R
759 (v. 4.2.2) by the k-means function with parameter nstart = 10 and using the silhouette function to
760 determine the optimal number of clusters. For motif enrichment analysis of ATAC-seq clusters, de
761 novo motifs were identified using Homer findMotifsGenome.pl (-size 200) with background peaks
762 consisting in the totality of ATAC-seq peaks retrieved (Table S3)

763 To quantify ATAC-seq read intensity at SWI/SNF regions in parental melanocytes and melanoma
764 cells, the matrix containing scores per genomic regions calculated with computeMatrix was
765 exported and plotted in R studio. Significance was calculated by Mann-Whitney U test using the
766 wilcox.test function in R. For ATAC-SWI/SNF correlation analysis, PBAF and BAF peaks were
767 selected to include only regions shared by fully formed complexes (i.e. ARID2, PBRM1 and BRG1
768 for PBAF; SS18 and BRG1 for BAF). Deeptools multiBigwigSummary was employed to generate
769 an enrichment matrix over the filtered PBAF or BAF regions and plotCorrelation function was used
770 to visualize plots and compute Spearman correlation.

771 **RNA-seq analysis.** Single-end 75-bp reads were aligned to the human reference genome
772 (hg38/GRCh38) with STAR (v. 2.7.5b)⁷⁴ using the parameters --runMode alignReads --
773 sjdbOverhang 100 --outFile- terMultimapNmax 10 --outFilterMismatchNmax 10 -- outFilterType
774 BySJout --outFilterIntronMotifs Remove- NoncanonicalUnannotated. Next, the featureCounts
775 function of the Rsubread R package (v. 3.19)⁷⁵ was used to assign reads to genes. Assigned
776 reads were then normalized and differential expression analysis was performed using the R
777 package DESeq2 (v. 1.38.3)⁷⁶. Genes were considered expressed if the sum of raw counts across
778 all samples was >10 for any given gene. Differentially expressed genes were called using
779 adjusted P-value of ≤0.05 and log₂FC of ≥0.75 or ≤-0.75. Volcano plots were generated with the

780 ggplot2 R package to depict DEseq2 results. Gene Ontology (GO) enrichment analysis was
781 performed on significantly up or downregulated genes using the Enrichr web server⁷⁷ and
782 selecting all expressed genes as background gene set. Transcription factor enrichment analysis
783 and GO Biological Processes categories were selected and adjusted p-values for the top terms
784 were shown as bar plots. The complete list of enriched terms is reported in Table S2.

785 **TCGA analysis.** Processed data from The Cancer Genome Atlas (TCGA - v. 28) were obtained
786 from the National Cancer Institute's Genomic Data Commons (GDC) Data Portal. The skin
787 cutaneous melanoma (SKCM) raw RNA-seq reads and mutational calls were downloaded using
788 the TCGAbiolinks (v.2.25.3) package⁷⁸. Sample normalization of raw counts was carried out using
789 the median-ratios normalization method from DESeq2 R package (v1.30.1, RRID:SCR_015687),
790 and differential expression analysis was performed using DESeq2. Genes with less than 5 reads
791 in total across all samples were considered not expressed and removed. Differentially expressed
792 genes were called using Benjamini-Hochberg adjusted p-value ≤ 0.05 and $\log_2FC \geq 0.5$ or ≤ -0.5 .
793 Over representation analysis (ORA) was performed using clusterProfiler (v4.2.2,
794 RRID:SCR_016884), on the Encode and ChEA consensus transcription factor gene set from the
795 Enrichr web server. Heatmaps depicting ORA analysis were generated using the pheatmap
796 (v1.0.12, RRID:SCR_016418) R package.

797

798 REFERENCES

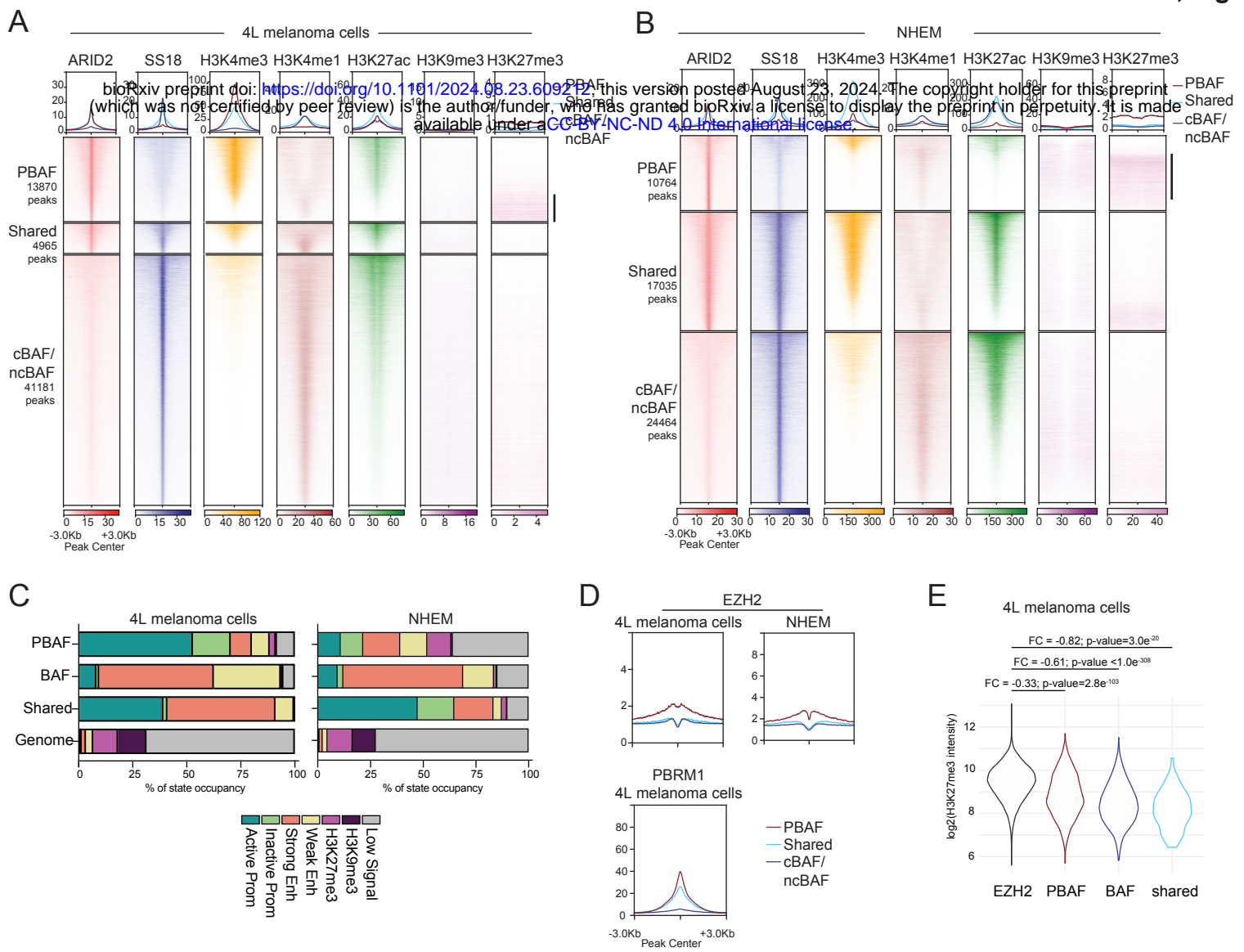
- 799 1. Hargreaves, D.C., and Crabtree, G.R. (2011). ATP-dependent chromatin remodeling:
800 genetics, genomics and mechanisms. *Cell Res* 21, 396-420. 10.1038/cr.2011.32.
- 801 2. Eustermann, S., Patel, A.B., Hopfner, K.P., He, Y., and Korber, P. (2024). Energy-driven
802 genome regulation by ATP-dependent chromatin remodellers. *Nat Rev Mol Cell Biol* 25,
803 309-332. 10.1038/s41580-023-00683-y.
- 804 3. He, S., Wu, Z., Tian, Y., Yu, Z., Yu, J., Wang, X., Li, J., Liu, B., and Xu, Y. (2020). Structure
805 of nucleosome-bound human BAF complex. *Science* 367, 875-881.
806 10.1126/science.aaz9761.
- 807 4. Mashtalir, N., Suzuki, H., Farrell, D.P., Sankar, A., Luo, J., Filipovski, M., D'Avino, A.R., St
808 Pierre, R., Valencia, A.M., Onikubo, T., et al. (2020). A Structural Model of the Endogenous
809 Human BAF Complex Informs Disease Mechanisms. *Cell* 183, 802-817 e824.
810 10.1016/j.cell.2020.09.051.
- 811 5. Yuan, J., Chen, K., Zhang, W., and Chen, Z. (2022). Structure of human chromatin-
812 remodelling PBAF complex bound to a nucleosome. *Nature* 605, 166-171.
813 10.1038/s41586-022-04658-5.
- 814 6. Mashtalir, N., D'Avino, A.R., Michel, B.C., Luo, J., Pan, J., Otto, J.E., Zullo, H.J.,
815 McKenzie, Z.M., Kubiak, R.L., St Pierre, R., et al. (2018). Modular Organization and
816 Assembly of SWI/SNF Family Chromatin Remodeling Complexes. *Cell* 175, 1272-1288
817 e1220. 10.1016/j.cell.2018.09.032.
- 818 7. Mashtalir, N., Dao, H.T., Sankar, A., Liu, H., Corin, A.J., Bagert, J.D., Ge, E.J., D'Avino,
819 A.R., Filipovski, M., Michel, B.C., et al. (2021). Chromatin landscape signals differentially
820 dictate the activities of mSWI/SNF family complexes. *Science* 373, 306-315.
821 10.1126/science.abf8705.
- 822 8. Ahmad, K., Brahma, S., and Henikoff, S. (2024). Epigenetic pioneering by SWI/SNF family
823 remodelers. *Mol Cell* 84, 194-201. 10.1016/j.molcel.2023.10.045.
- 824 9. Brahma, S., and Henikoff, S. (2024). The BAF chromatin remodeler synergizes with RNA
825 polymerase II and transcription factors to evict nucleosomes. *Nat Genet* 56, 100-111.
826 10.1038/s41588-023-01603-8.
- 827 10. Barisic, D., Stadler, M.B., Iurlaro, M., and Schubeler, D. (2019). Mammalian ISWI and
828 SWI/SNF selectively mediate binding of distinct transcription factors. *Nature* 569, 136-140.
829 10.1038/s41586-019-1115-5.
- 830 11. Schick, S., Grosche, S., Kohl, K.E., Drpic, D., Jaeger, M.G., Marella, N.C., Imrichova, H.,
831 Lin, J.G., Hofstatter, G., Schuster, M., et al. (2021). Acute BAF perturbation causes
832 immediate changes in chromatin accessibility. *Nat Genet* 53, 269-278. 10.1038/s41588-
833 021-00777-3.
- 834 12. Iurlaro, M., Stadler, M.B., Masoni, F., Jagani, Z., Galli, G.G., and Schubeler, D. (2021).
835 Mammalian SWI/SNF continuously restores local accessibility to chromatin. *Nat Genet* 53,
836 279-287. 10.1038/s41588-020-00768-w.
- 837 13. Basurto-Cayuela, L., Guerrero-Martinez, J.A., Gomez-Marin, E., Sanchez-Escabias, E.,
838 Escano-Maestre, M., Ceballos-Chavez, M., and Reyes, J.C. (2024). SWI/SNF-dependent
839 genes are defined by their chromatin landscape. *Cell Rep* 43, 113855.
840 10.1016/j.celrep.2024.113855.
- 841 14. Martin, B.J.E., Ablondi, E.F., Goglia, C., Mimoso, C.A., Espinel-Cabrera, P.R., and
842 Adelman, K. (2023). Global identification of SWI/SNF targets reveals compensation by
843 EP400. *Cell* 186, 5290-5307 e5226. 10.1016/j.cell.2023.10.006.
- 844 15. Kadoch, C., Williams, R.T., Calarco, J.P., Miller, E.L., Weber, C.M., Braun, S.M., Pulice,
845 J.L., Chory, E.J., and Crabtree, G.R. (2017). Dynamics of BAF-Polycomb complex
846 opposition on heterochromatin in normal and oncogenic states. *Nat Genet* 49, 213-222.
847 10.1038/ng.3734.

- 848 16. Weber, C.M., Hafner, A., Kirkland, J.G., Braun, S.M.G., Stanton, B.Z., Boettiger, A.N., and
849 Crabtree, G.R. (2021). mSWI/SNF promotes Polycomb repression both directly and
850 through genome-wide redistribution. *Nat Struct Mol Biol* 28, 501-511. 10.1038/s41594-
851 021-00604-7.
- 852 17. Nakayama, R.T., Pulice, J.L., Valencia, A.M., McBride, M.J., McKenzie, Z.M., Gillespie,
853 M.A., Ku, W.L., Teng, M., Cui, K., Williams, R.T., et al. (2017). SMARCB1 is required for
854 widespread BAF complex-mediated activation of enhancers and bivalent promoters. *Nat*
855 *Genet* 49, 1613-1623. 10.1038/ng.3958.
- 856 18. Kadoch, C., Hargreaves, D.C., Hodges, C., Elias, L., Ho, L., Ranish, J., and Crabtree,
857 G.R. (2013). Proteomic and bioinformatic analysis of mammalian SWI/SNF complexes
858 identifies extensive roles in human malignancy. *Nat Genet* 45, 592-601. 10.1038/ng.2628.
- 859 19. Shain, A.H., and Pollack, J.R. (2013). The spectrum of SWI/SNF mutations, ubiquitous in
860 human cancers. *PLoS One* 8, e55119. 10.1371/journal.pone.0055119.
- 861 20. Mittal, P., and Roberts, C.W.M. (2020). The SWI/SNF complex in cancer - biology,
862 biomarkers and therapy. *Nat Rev Clin Oncol* 17, 435-448. 10.1038/s41571-020-0357-3.
- 863 21. Hodis, E., Watson, I.R., Kryukov, G.V., Arold, S.T., Imielinski, M., Theurillat, J.P.,
864 Nickerson, E., Auclair, D., Li, L., Place, C., et al. (2012). A landscape of driver mutations
865 in melanoma. *Cell* 150, 251-263. 10.1016/j.cell.2012.06.024.
- 866 22. Shain, A.H., Joseph, N.M., Yu, R., Benhamida, J., Liu, S., Prow, T., Ruben, B., North, J.,
867 Pincus, L., Yeh, I., et al. (2018). Genomic and Transcriptomic Analysis Reveals
868 Incremental Disruption of Key Signaling Pathways during Melanoma Evolution. *Cancer*
869 *Cell* 34, 45-55 e44. 10.1016/j.ccell.2018.06.005.
- 870 23. Tang, J., Fewings, E., Chang, D., Zeng, H., Liu, S., Jorapur, A., Belote, R.L., McNeal, A.S.,
871 Tan, T.M., Yeh, I., et al. (2020). The genomic landscapes of individual melanocytes from
872 human skin. *Nature* 586, 600-605. 10.1038/s41586-020-2785-8.
- 873 24. Martinez-Jimenez, F., Muinos, F., Sentis, I., Deu-Pons, J., Reyes-Salazar, I., Arnedo-Pac,
874 C., Mularoni, L., Pich, O., Bonet, J., Kranas, H., et al. (2020). A compendium of mutational
875 cancer driver genes. *Nat Rev Cancer* 20, 555-572. 10.1038/s41568-020-0290-x.
- 876 25. Cerami, E., Gao, J., Dogrusoz, U., Gross, B.E., Sumer, S.O., Aksoy, B.A., Jacobsen, A.,
877 Byrne, C.J., Heuer, M.L., Larsson, E., et al. (2012). The cBio cancer genomics portal: an
878 open platform for exploring multidimensional cancer genomics data. *Cancer Discov* 2,
879 401-404. 10.1158/2159-8290.CD-12-0095.
- 880 26. Gao, J., Aksoy, B.A., Dogrusoz, U., Dresdner, G., Gross, B., Sumer, S.O., Sun, Y.,
881 Jacobsen, A., Sinha, R., Larsson, E., et al. (2013). Integrative analysis of complex cancer
882 genomics and clinical profiles using the cBioPortal. *Sci Signal* 6, pi1.
883 10.1126/scisignal.2004088.
- 884 27. Cancer Genome Atlas, N. (2015). Genomic Classification of Cutaneous Melanoma. *Cell*
885 161, 1681-1696. 10.1016/j.cell.2015.05.044.
- 886 28. In, G.K., Poorman, K., Saul, M., O'Day, S., Farma, J.M., Olszanski, A.J., Gordon, M.S.,
887 Thomas, J.S., Eisenberg, B., Flaherty, L., et al. (2020). Molecular profiling of melanoma
888 brain metastases compared to primary cutaneous melanoma and to extracranial
889 metastases. *Oncotarget* 11, 3118-3128. 10.18632/oncotarget.27686.
- 890 29. Varaljai, R., Horn, S., Sucker, A., Piercianek, D., Schmitt, V., Carpinteiro, A., Becker, K.A.,
891 Reifenberger, J., Roesch, A., Felsberg, J., et al. (2021). Integrative Genomic Analyses of
892 Patient-Matched Intracranial and Extracranial Metastases Reveal a Novel Brain-Specific
893 Landscape of Genetic Variants in Driver Genes of Malignant Melanoma. *Cancers (Basel)*
894 13. 10.3390/cancers13040731.
- 895 30. Carcamo, S., Nguyen, C.B., Grossi, E., Filipescu, D., Alpsoy, A., Dhiman, A., Sun, D.,
896 Narang, S., Imig, J., Martin, T.C., et al. (2022). Altered BAF occupancy and transcription
897 factor dynamics in PBAF-deficient melanoma. *Cell Rep* 39, 110637.
898 10.1016/j.celrep.2022.110637.

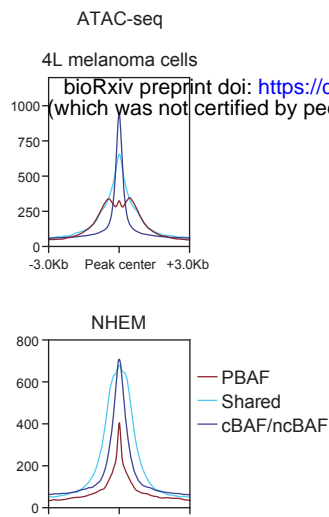
- 899 31. Ang, Y.S., Tsai, S.Y., Lee, D.F., Monk, J., Su, J., Ratnakumar, K., Ding, J., Ge, Y., Darr, H.,
900 Chang, B., et al. (2011). Wdr5 mediates self-renewal and reprogramming via the
901 embryonic stem cell core transcriptional network. *Cell* 145, 183-197.
902 10.1016/j.cell.2011.03.003.
- 903 32. Gu, B., and Lee, M.G. (2013). Histone H3 lysine 4 methyltransferases and demethylases
904 in self-renewal and differentiation of stem cells. *Cell Biosci* 3, 39. 10.1186/2045-3701-3-
905 39.
- 906 33. Ernst, J., and Kellis, M. (2017). Chromatin-state discovery and genome annotation with
907 ChromHMM. *Nat Protoc* 12, 2478-2492. 10.1038/nprot.2017.124.
- 908 34. Gaspar-Maia, A., Alajem, A., Meshorer, E., and Ramalho-Santos, M. (2011). Open
909 chromatin in pluripotency and reprogramming. *Nat Rev Mol Cell Biol* 12, 36-47.
910 10.1038/nrm3036.
- 911 35. Lessard, J., Wu, J.I., Ranish, J.A., Wan, M., Winslow, M.M., Staahl, B.T., Wu, H.,
912 Aebersold, R., Graef, I.A., and Crabtree, G.R. (2007). An essential switch in subunit
913 composition of a chromatin remodeling complex during neural development. *Neuron* 55,
914 201-215. 10.1016/j.neuron.2007.06.019.
- 915 36. Billaud, M., and Santoro, M. (2011). Is Co-option a prevailing mechanism during cancer
916 progression? *Cancer Res* 71, 6572-6575. 10.1158/0008-5472.CAN-11-2158.
- 917 37. Logotheti, S., Marquardt, S., Richter, C., Sophie Hain, R., Murr, N., Takan, I., Pavlopoulou,
918 A., and Putzer, B.M. (2020). Neural Networks Recapitulation by Cancer Cells Promotes
919 Disease Progression: A Novel Role of p73 Isoforms in Cancer-Neuronal Crosstalk.
920 *Cancers (Basel)* 12. 10.3390/cancers12123789.
- 921 38. Venkatesh, H.S., Morishita, W., Geraghty, A.C., Silverbush, D., Gillespie, S.M., Arzt, M.,
922 Tam, L.T., Espenel, C., Ponnuswami, A., Ni, L., et al. (2019). Electrical and synaptic
923 integration of glioma into neural circuits. *Nature* 573, 539-545. 10.1038/s41586-019-1563-
924 y.
- 925 39. Biermann, J., Melms, J.C., Amin, A.D., Wang, Y., Caprio, L.A., Karz, A., Tagore, S.,
926 Barrera, I., Ibarra-Arellano, M.A., Andreatta, M., et al. (2022). Dissecting the treatment-
927 naive ecosystem of human melanoma brain metastasis. *Cell* 185, 2591-2608 e2530.
928 10.1016/j.cell.2022.06.007.
- 929 40. Papillon, J.P.N., Nakajima, K., Adair, C.D., Hempel, J., Jouk, A.O., Karki, R.G., Mathieu,
930 S., Mobitz, H., Ntaganda, R., Smith, T., et al. (2018). Discovery of Orally Active Inhibitors
931 of Brahma Homolog (BRM)/SMARCA2 ATPase Activity for the Treatment of Brahma
932 Related Gene 1 (BRG1)/SMARCA4-Mutant Cancers. *J Med Chem* 61, 10155-10172.
933 10.1021/acs.jmedchem.8b01318.
- 934 41. Chong, J.A., Tapia-Ramirez, J., Kim, S., Toledo-Aral, J.J., Zheng, Y., Boutros, M.C.,
935 Altshuler, Y.M., Frohman, M.A., Kraner, S.D., and Mandel, G. (1995). REST: a mammalian
936 silencer protein that restricts sodium channel gene expression to neurons. *Cell* 80, 949-
937 957. 10.1016/0092-8674(95)90298-8.
- 938 42. Hwang, J.Y., and Zukin, R.S. (2018). REST, a master transcriptional regulator in
939 neurodegenerative disease. *Curr Opin Neurobiol* 48, 193-200.
940 10.1016/j.conb.2017.12.008.
- 941 43. Ooi, L., and Wood, I.C. (2007). Chromatin crosstalk in development and disease: lessons
942 from REST. *Nat Rev Genet* 8, 544-554. 10.1038/nrg2100.
- 943 44. Schoenherr, C.J., and Anderson, D.J. (1995). The neuron-restrictive silencer factor
944 (NRSF): a coordinate repressor of multiple neuron-specific genes. *Science* 267, 1360-
945 1363. 10.1126/science.7871435.
- 946 45. Sehgal, P., and Chaturvedi, P. (2023). Chromatin and Cancer: Implications of Disrupted
947 Chromatin Organization in Tumorigenesis and Its Diversification. *Cancers (Basel)* 15.
948 10.3390/cancers15020466.

- 949 46. Bergwell, M., Park, J., and Kirkland, J.G. (2024). Differential Modulation of Polycomb-
950 Associated Histone Marks by cBAF, pBAF, and gBAF Complexes. *bioRxiv*.
951 10.1101/2023.09.23.557848.
- 952 47. Wang, L., Yu, J., Yu, Z., Wang, Q., Li, W., Ren, Y., Chen, Z., He, S., and Xu, Y. (2022).
953 Structure of nucleosome-bound human PBAF complex. *Nat Commun* 13, 7644.
954 10.1038/s41467-022-34859-5.
- 955 48. Cheli, Y., Ohanna, M., Ballotti, R., and Bertolotto, C. (2010). Fifteen-year quest for
956 microphthalmia-associated transcription factor target genes. *Pigment Cell Melanoma Res*
957 23, 27-40. 10.1111/j.1755-148X.2009.00653.x.
- 958 49. Seberg, H.E., Van Otterloo, E., and Cornell, R.A. (2017). Beyond MITF: Multiple
959 transcription factors directly regulate the cellular phenotype in melanocytes and
960 melanoma. *Pigment Cell Melanoma Res* 30, 454-466. 10.1111/pcmr.12611.
- 961 50. Stadler, M.B., Murr, R., Burger, L., Ivanek, R., Lienert, F., Scholer, A., van Nimwegen, E.,
962 Wirbelauer, C., Oakeley, E.J., Gaidatzis, D., et al. (2011). DNA-binding factors shape the
963 mouse methylome at distal regulatory regions. *Nature* 480, 490-495.
964 10.1038/nature10716.
- 965 51. Iurlaro, M., Masoni, F., Flyamer, I.M., Wirbelauer, C., Iskar, M., Burger, L., Giorgetti, L.,
966 and Schubeler, D. (2024). Systematic assessment of ISWI subunits shows that NURF
967 creates local accessibility for CTCF. *Nat Genet*. 10.1038/s41588-024-01767-x.
- 968 52. Jin, L., Liu, Y., Wu, Y., Huang, Y., and Zhang, D. (2023). REST Is Not Resting: REST/NRSF
969 in Health and Disease. *Biomolecules* 13. 10.3390/biom13101477.
- 970 53. Erickson, C.A. (1993). From the crest to the periphery: control of pigment cell migration
971 and lineage segregation. *Pigment Cell Res* 6, 336-347. 10.1111/j.1600-
972 0749.1993.tb00611.x.
- 973 54. Aoki, H., Hara, A., and Kunisada, T. (2015). White spotting phenotype induced by targeted
974 REST disruption during neural crest specification to a melanocyte cell lineage. *Genes*
975 *Cells* 20, 439-449. 10.1111/gtc.12235.
- 976 55. Bajpai, R., Chen, D.A., Rada-Iglesias, A., Zhang, J., Xiong, Y., Helms, J., Chang, C.P.,
977 Zhao, Y., Swigut, T., and Wysocka, J. (2010). CHD7 cooperates with PBAF to control
978 multipotent neural crest formation. *Nature* 463, 958-962. 10.1038/nature08733.
- 979 56. Torroglosa, A., Villalba-Benito, L., Luzon-Toro, B., Fernandez, R.M., Antinolo, G., and
980 Borrego, S. (2019). Epigenetic Mechanisms in Hirschsprung Disease. *Int J Mol Sci* 20.
981 10.3390/ijms20133123.
- 982 57. Tagore, M., Hergenreder, E., Perlee, S.C., Cruz, N.M., Menocal, L., Suresh, S., Chan, E.,
983 Baron, M., Melendez, S., Dave, A., et al. (2023). GABA Regulates Electrical Activity and
984 Tumor Initiation in Melanoma. *Cancer Discov* 13, 2270-2291. 10.1158/2159-8290.CD-23-
985 0389.
- 986 58. Wang, H., Zheng, Q., Lu, Z., Wang, L., Ding, L., Xia, L., Zhang, H., Wang, M., Chen, Y.,
987 and Li, G. (2021). Role of the nervous system in cancers: a review. *Cell Death Discov* 7,
988 76. 10.1038/s41420-021-00450-y.
- 989 59. Fontanals-Cirera, B., Hasson, D., Vardabasso, C., Di Micco, R., Agrawal, P., Chowdhury,
990 A., Gantz, M., de Pablos-Aragoneses, A., Morgenstern, A., Wu, P., et al. (2017).
991 Harnessing BET Inhibitor Sensitivity Reveals AMIGO2 as a Melanoma Survival Gene. *Mol*
992 *Cell* 68, 731-744 e739. 10.1016/j.molcel.2017.11.004.
- 993 60. Vardabasso, C., Gaspar-Maia, A., Hasson, D., Punzeler, S., Valle-Garcia, D., Straub, T.,
994 Keilhauer, E.C., Strub, T., Dong, J., Panda, T., et al. (2015). Histone Variant H2A.Z.2
995 Mediates Proliferation and Drug Sensitivity of Malignant Melanoma. *Mol Cell* 59, 75-88.
996 10.1016/j.molcel.2015.05.009.
- 997 61. Alpsy, A., and Dykhuizen, E.C. (2018). Glioma tumor suppressor candidate region gene
998 1 (GLTSCR1) and its paralog GLTSCR1-like form SWI/SNF chromatin remodeling
999 subcomplexes. *J Biol Chem* 293, 3892-3903. 10.1074/jbc.RA117.001065.

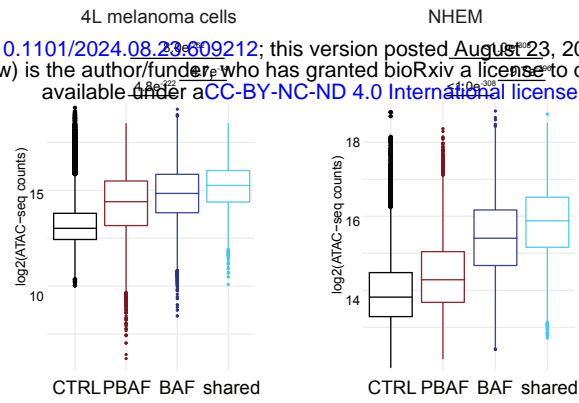
- 1000 62. Corces, M.R., Trevino, A.E., Hamilton, E.G., Greenside, P.G., Sinnott-Armstrong, N.A.,
1001 Vesuna, S., Satpathy, A.T., Rubin, A.J., Montine, K.S., Wu, B., et al. (2017). An improved
1002 ATAC-seq protocol reduces background and enables interrogation of frozen tissues. *Nat*
1003 *Methods* 14, 959-962. 10.1038/nmeth.4396.
- 1004 63. Bolger, A.M., Lohse, M., and Usadel, B. (2014). Trimmomatic: a flexible trimmer for
1005 Illumina sequence data. *Bioinformatics* 30, 2114-2120. 10.1093/bioinformatics/btu170.
- 1006 64. Gaspar, J.M. (2018). NGmerge: merging paired-end reads via novel empirically-derived
1007 models of sequencing errors. *BMC Bioinformatics* 19, 536. 10.1186/s12859-018-2579-2.
- 1008 65. Langmead, B., and Salzberg, S.L. (2012). Fast gapped-read alignment with Bowtie 2. *Nat*
1009 *Methods* 9, 357-359. 10.1038/nmeth.1923.
- 1010 66. Danecek, P., Bonfield, J.K., Liddle, J., Marshall, J., Ohan, V., Pollard, M.O., Whitwham, A.,
1011 Keane, T., McCarthy, S.A., Davies, R.M., and Li, H. (2021). Twelve years of SAMtools and
1012 BCFtools. *Gigascience* 10. 10.1093/gigascience/giab008.
- 1013 67. Zhang, Y., Liu, T., Meyer, C.A., Eeckhoute, J., Johnson, D.S., Bernstein, B.E., Nusbaum,
1014 C., Myers, R.M., Brown, M., Li, W., and Liu, X.S. (2008). Model-based analysis of ChIP-
1015 Seq (MACS). *Genome Biol* 9, R137. 10.1186/gb-2008-9-9-r137.
- 1016 68. Zang, C., Schones, D.E., Zeng, C., Cui, K., Zhao, K., and Peng, W. (2009). A clustering
1017 approach for identification of enriched domains from histone modification ChIP-Seq data.
1018 *Bioinformatics* 25, 1952-1958. 10.1093/bioinformatics/btp340.
- 1019 69. Ramirez, F., Ryan, D.P., Gruning, B., Bhardwaj, V., Kilpert, F., Richter, A.S., Heyne, S.,
1020 Dundar, F., and Manke, T. (2016). deepTools2: a next generation web server for deep-
1021 sequencing data analysis. *Nucleic Acids Res* 44, W160-165. 10.1093/nar/gkw257.
- 1022 70. Quinlan, A.R., and Hall, I.M. (2010). BEDTools: a flexible suite of utilities for comparing
1023 genomic features. *Bioinformatics* 26, 841-842. 10.1093/bioinformatics/btq033.
- 1024 71. Wang, Q., Li, M., Wu, T., Zhan, L., Li, L., Chen, M., Xie, W., Xie, Z., Hu, E., Xu, S., and Yu,
1025 G. (2022). Exploring Epigenomic Datasets by ChIPseeker. *Curr Protoc* 2, e585.
1026 10.1002/cpz1.585.
- 1027 72. Ernst, J., and Kellis, M. (2012). ChromHMM: automating chromatin-state discovery and
1028 characterization. *Nat Methods* 9, 215-216. 10.1038/nmeth.1906.
- 1029 73. Ross-Innes, C.S., Stark, R., Teschendorff, A.E., Holmes, K.A., Ali, H.R., Dunning, M.J.,
1030 Brown, G.D., Gojis, O., Ellis, I.O., Green, A.R., et al. (2012). Differential oestrogen receptor
1031 binding is associated with clinical outcome in breast cancer. *Nature* 481, 389-393.
1032 10.1038/nature10730.
- 1033 74. Dobin, A., Davis, C.A., Schlesinger, F., Drenkow, J., Zaleski, C., Jha, S., Batut, P.,
1034 Chaisson, M., and Gingeras, T.R. (2013). STAR: ultrafast universal RNA-seq aligner.
1035 *Bioinformatics* 29, 15-21. 10.1093/bioinformatics/bts635.
- 1036 75. Liao, Y., Smyth, G.K., and Shi, W. (2019). The R package Rsubread is easier, faster,
1037 cheaper and better for alignment and quantification of RNA sequencing reads. *Nucleic*
1038 *Acids Res* 47, e47. 10.1093/nar/gkz114.
- 1039 76. Love, M.I., Huber, W., and Anders, S. (2014). Moderated estimation of fold change and
1040 dispersion for RNA-seq data with DESeq2. *Genome Biol* 15, 550. 10.1186/s13059-014-
1041 0550-8.
- 1042 77. Kuleshov, M.V., Jones, M.R., Rouillard, A.D., Fernandez, N.F., Duan, Q., Wang, Z., Koplev,
1043 S., Jenkins, S.L., Jagodnik, K.M., Lachmann, A., et al. (2016). Enrichr: a comprehensive
1044 gene set enrichment analysis web server 2016 update. *Nucleic Acids Res* 44, W90-97.
1045 10.1093/nar/gkw377.
- 1046 78. Mounir, M., Lucchetta, M., Silva, T.C., Olsen, C., Bontempi, G., Chen, X., Noushmehr, H.,
1047 Colaprico, A., and Papaleo, E. (2019). New functionalities in the TCGAbiolinks package
1048 for the study and integration of cancer data from GDC and GTEx. *PLoS Comput Biol* 15,
1049 e1006701. 10.1371/journal.pcbi.1006701.



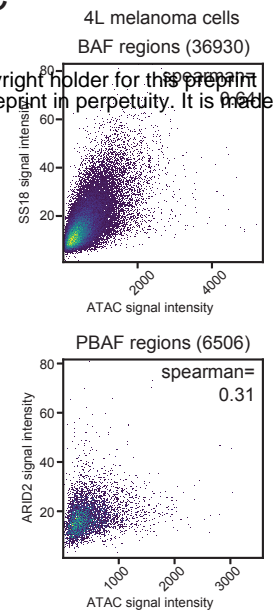
A



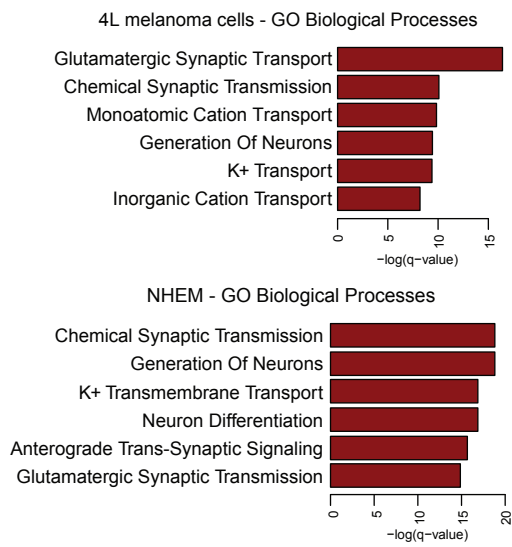
B



C



D



E

